Matching pursuit for imaging high-contrast conductivity

To cite this article: Liliana Borcea *et al* 1999 *Inverse Problems* **15** 811

Inverse Problems **15** (1999) 811–849. Printed in the UK PII: S0266-5611(99)98369-7

Matching pursuit for imaging high-contrast conductivity

Liliana Borcea†, James G Berryman‡ and George C Papanicolaou§

† Computational and Applied Mathematics, MS 134, Rice University, 6100 Main Street, Houston, TX 77005-1892, USA

‡ Lawrence Livermore National Laboratories, PO Box 808 L-200, Livermore, CA 94551-9900, USA

§ Department of Mathematics, Stanford University, Stanford, CA 94305, USA

E-mail: borcea@caam.rice.edu, berryman@s123.es.llnl.gov and papanicolaou@stanford.edu

Received 14 October 1998, in final form 16 March 1999

Abstract. We show that imaging an isotropic, high contrast, conductive medium is asymptotically equivalent to the identification of a unique resistor network, given measurements of currents and voltages at the boundary. We show that a matching pursuit approach can be used effectively towards the numerical solution of the high-contrast imaging problem, if the library of functions is constructed carefully and in accordance with the asymptotic theory. We also show how other libraries of functions that at first glance seem reasonable, in fact, do not work well. When the contrast in the conductivity is not so high, we show that wavelets can be used, especially non-orthogonal wavelet libraries. However, the library of functions that is based on the high-contrast asymptotic theory is more robust, even for intermediate contrasts, and especially so in the presence of noise.

1. Introduction

We consider an inhomogeneous conducting material in a simply connected domain $\Omega \in \mathbb{R}^2$. The electric potential ϕ satisfies the boundary value problem

$$\begin{aligned} &\nabla \cdot [\sigma(\boldsymbol{x})\nabla\phi(\boldsymbol{x})] = 0 \qquad \text{in } \Omega \\ &\sigma \frac{\partial \phi(\boldsymbol{x})}{\partial n} = I(\boldsymbol{x}) \qquad \text{on } \partial\Omega \\ &\int_{\partial\Omega} I \, \mathrm{d}s = 0 \end{aligned} \tag{1.1}$$

where σ is the electrical conductivity and I is the normal current density given at the boundary. In impedance tomography, $\sigma(\boldsymbol{x})$ is unknown and it is to be found from simultaneous measurements of currents and voltages at the boundary. Thus, for a given current excitation I, we overspecify the problem (1.1) by requiring that

$$\phi(\boldsymbol{x}) = \psi(\boldsymbol{x}) \qquad \text{on } \partial\Omega \tag{1.2}$$

where ψ is the measured voltage at the boundary. When all possible excitations and measurements at the boundary are available, we know the Neumann to Dirichlet (NtD) map which maps current I into voltages ψ. The mathematical problem of impedance tomography is: find σ in the interior of Ω from the NtD map. In practice, we rarely have the full NtD map available, so the imaging has to be done with partial information about it. The inverse

0266-5611/99/040811+39$30.00

problem can also be formulated in terms of the Dirichlet to Neumann (DtN) map which maps voltages into currents. Thus, we can design our data gathering experiments so that we specify the voltage at the boundary and measure currents. However, in practice, it is more advantageous to work with the NtD map because it is smoothing and so, the data are less noisy.

In this paper we consider imaging a function σ that includes high contrast, which means that the ratio of its maximum to its minimum value is large. There are many ways in which high contrast may arise in conducting media. We concentrate on media with insulating or highly conducting inclusions in a smooth background. Since in most applications we do not have detailed information about the medium, such as shape of inclusions, we model high contrast conductivity as a continuous function given by [9, 10, 31]

$$\sigma(\boldsymbol{x}) = \sigma_0 \, \mathrm{e}^{-S(\boldsymbol{x})/\epsilon} \tag{1.3}$$

where σ_0 is constant, $S(\boldsymbol{x})$ is a smooth function with isolated, non-degenerate critical points (Morse function) and ϵ is a small and positive parameter. Thus, as ϵ decreases, the contrast of σ becomes exponentially large. Clearly, the inverse problem for such high-contrast media is highly nonlinear and the usual imaging methods based on linearization [12, 17, 41] are not expected to work. Moreover, the theoretical results [23, 24, 38, 39] that ensure unique determination of the conductivity from the NtD map fail in the high-contrast limit. In this paper we show how the high-contrast asymptotic theory introduced in [10, 31] can be used to overcome the difficulties of the highly nonlinear inverse problem, leading to a matching pursuit method with a special library of functions. We also compare the performance of this library of functions to others, such as wavelets, which are not based on the high-contrast asymptotics. Our numerical experiments suggest that the high-contrast library gives better and more efficient reconstructions, even when the contrast is not so high and the data are noisy.

The idea of using the high-contrast asymptotic theory in imaging was introduced in [9]. However, we did not explain the theoretical basis of the inversion method and did not address the issue of uniqueness of the image. Moreover, the numerical experiments were limited and we did not compare high-contrast imaging with results obtained with other libraries of functions. In this paper we address these issues. In section 3 we show that, in the asymptotic limit of very high contrast, the imaging problem is asymptotically equivalent to the identification of a resistor network from measurements of the potential at the peripheral nodes and given input/output currents. Thus, as shown in [14, 15, 18], the high-contrast features of $\sigma(\boldsymbol{x})$ that are contained in the asymptotic resistor network approximation [10, 31] can be uniquely recovered in general. In section 4 we give a detailed description of the library of functions, based on the high-contrast asymptotic theory, that we use for inversion. In section 5 we present numerical results that assess the efficiency and robustness of the high-contrast library. In section 6 we discuss other libraries of functions, such as Gaussians and wavelets. We present numerical results and compare with the performance of the high-contrast library introduced in section 4. We end with a brief summary and conclusions.

2. The Neumann to Dirichlet map for a continuum

Since the imaging problem is to determine the conductivity in the domain Ω given partial knowledge of the NtD or DtN maps, we need to know how the maps behave as the contrast in the medium increases, that is as ϵ goes to zero. The DtN map is defined by

$$\Lambda^\epsilon \psi = \sigma \frac{\partial \phi}{\partial n}\bigg|_{\partial\Omega} = I(\boldsymbol{x}) \tag{2.1}$$

where σ is given by (1.3), ϕ is the solution of

$$\begin{aligned} &\nabla \cdot [\sigma_0 \, \mathrm{e}^{-S(\boldsymbol{x})/\epsilon} \nabla \phi(\boldsymbol{x})] = 0 \qquad \text{in } \Omega \\ &\phi(\boldsymbol{x}) = \psi(\boldsymbol{x}) \qquad \text{on } \partial\Omega \end{aligned} \tag{2.2}$$

and $\boldsymbol{n}$ is the unit outer normal to $\partial\Omega$. If the potential at the boundary is in $H^{1/2}(\partial\Omega)$, then $I = \Lambda^\epsilon \psi$ is in $H^{-1/2}(\partial\Omega)$ and the inner product

$$(\psi, \Lambda^\epsilon \psi) = \int_{\partial\Omega} I(\boldsymbol{x}) \psi(\boldsymbol{x}) \, \mathrm{d}s \tag{2.3}$$

is well defined. The DtN map is self-adjoint and positive semidefinite [38], as can be seen by using Green's theorem. Furthermore, from Green's theorem and (2.2), one can also obtain the variational formulation [13]

$$(\psi, \Lambda^\epsilon \psi) = \min_{\phi|_{\partial\Omega} = \psi} \int_\Omega \sigma_0 \, \mathrm{e}^{-S(\boldsymbol{x})/\epsilon} \nabla \phi(\boldsymbol{x}) \cdot \nabla \phi(\boldsymbol{x}) \, \mathrm{d}\boldsymbol{x} \tag{2.4}$$

for the quadratic form (2.3). Finally, Λ^ϵ has a null space spanned by the constant functions ψ.

The generalized inverse of the map Λ^ϵ, the NtD map

$$(\Lambda^\epsilon)^{-1} I = \psi \tag{2.5}$$

is defined on the restricted space of currents $I \in H^{-1/2}(\partial\Omega)$ that satisfy $\int_{\partial\Omega} I(\boldsymbol{x}) \, \mathrm{d}s = 0$. The NtD map is self-adjoint and positive definite. In fact, by using Green's theorem, we obtain

$$(I, (\Lambda^\epsilon)^{-1} I) = \int_{\partial\Omega} I(\boldsymbol{x}) \psi(\boldsymbol{x}) \, \mathrm{d}s = \int_\Omega \sigma_0 \, \mathrm{e}^{-S(\boldsymbol{x})/\epsilon} \nabla \phi \cdot \nabla \phi \, \mathrm{d}\boldsymbol{x} \tag{2.6}$$

where ϕ is the solution of problem (1.1), with σ given by (1.3). The current density is given by

$$\boldsymbol{j}(\boldsymbol{x}) = -\sigma_0 \, \mathrm{e}^{-S(\boldsymbol{x})/\epsilon} \nabla \phi(\boldsymbol{x}) \qquad \text{for } \boldsymbol{x} \in \Omega \tag{2.7}$$

where $\boldsymbol{j}(\boldsymbol{x})$ satisfies

$$\begin{aligned} &\nabla \times \left[\frac{1}{\sigma_0} \, \mathrm{e}^{S(\boldsymbol{x})/\epsilon} \boldsymbol{j}(\boldsymbol{x}) \right] = 0 \\ &\nabla \cdot \boldsymbol{j}(\boldsymbol{x}) = 0 \qquad \text{for } \boldsymbol{x} \in \Omega \\ &-\boldsymbol{n} \cdot \boldsymbol{j} = I \qquad \text{on } \partial\Omega. \end{aligned} \tag{2.8}$$

Thus, (2.6) can be rewritten in terms of the current density $\boldsymbol{j}$ and, because of equation (2.8), we have the variational formulation (see [13]):

$$(I, (\Lambda^\epsilon)^{-1} I) = \min_{\nabla \cdot \boldsymbol{j} = 0; \, -\boldsymbol{j} \cdot \boldsymbol{n}|_{\partial\Omega} = I} \int_\Omega \frac{1}{\sigma_0} \, \mathrm{e}^{S(\boldsymbol{x})/\epsilon} \boldsymbol{j}(\boldsymbol{x}) \cdot \boldsymbol{j}(\boldsymbol{x}) \, \mathrm{d}\boldsymbol{x} \tag{2.9}$$

where $\int_{\partial\Omega} I \, \mathrm{d}s = 0$.

3. High-contrast asymptotics

3.1. Asymptotic resistor network approximation

The asymptotic analysis of the direct problem

$$\begin{aligned} &\nabla \cdot (\sigma_0 \, \mathrm{e}^{-S/\epsilon} \nabla \phi) = 0 \qquad \text{in } \Omega \\ &\sigma_0 \, \mathrm{e}^{-S/\epsilon} \frac{\partial \phi}{\partial n} = I \qquad \text{on } \partial\Omega \\ &\int_{\partial\Omega} I \, \mathrm{d}s = 0 \end{aligned} \tag{3.1}$$

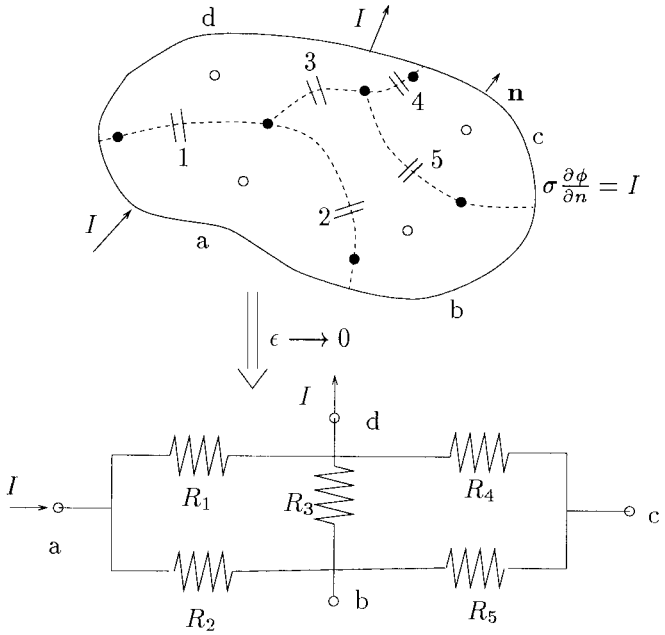

Figure 1. Example of an asymptotically equivalent resistor network.

in media with conductivity given by (1.3), shows that the flow of current concentrates at local maxima and saddle points of $\sigma(\boldsymbol{x})$ [9, 10, 31]. Furthermore, the potential gradient is small at maxima of $\sigma(\boldsymbol{x})$ and large at saddle points of the electrical conductivity. Thus, small neighbourhoods of the saddle points of $\sigma(\boldsymbol{x})$ in the domain Ω of the solution give the main contribution to the power dissipated into heat in the material. With each saddle point or channel of flow concentration, we can associate a resistor and then, approximate transport in the high-contrast medium by current flow in a resistor network that is determined as follows. The nodes of the network are maxima of $\sigma(\boldsymbol{x})$ and the branches connect two adjacent maxima through a saddle. The resistance associated with each saddle point of $S(\boldsymbol{x})$ has the form

$$R = \frac{1}{\sigma(\boldsymbol{x}_s)}\sqrt{\frac{k_+}{k_-}} \tag{3.2}$$

where k_+ and k_- are the curvatures of S at the saddle point $\boldsymbol{x}_s$ (see [9, 10, 31]).

In figure 1 we show an example of how the asymptotic resistor network is constructed. We consider a continuum with a high-contrast conductivity that has four maxima and six minima shown in the figure by $\circ$ and $\bullet$, respectively. There are also five saddle points of σ denoted in the figure by $1, \ldots, 5$. The current flows along paths of maximal conductivity. Hence, the current avoids minima of the conductivity and it is attracted by the maxima of σ. Each maximum of σ has a basin of attraction delimited in Ω by the ridge of minimal conductivity passing through the neighbouring saddle points (see dotted curves in figure 1). Due to the external driving, the current must flow from one maximum of σ to another, where the least resistive path goes through the saddle points. When the contrast of σ is high, the current is strongly concentrated along the paths of maximal conductivity and so it flows like current in a resistor network. The branches of the network connect adjacent maxima of σ through the saddle points. Hence, in figure 1 we have five branches, each one carrying a

resistance R_i, $i = 1, \ldots, 5$. Finally, to draw the asymptotic network, we must determine its peripheral nodes. Previous analysis [10, 31] considers flow in periodic media and so it does not address the issue of boundary conditions. Heuristically, we expect to have four peripheral nodes a, b, c and d, one for each maximum of σ near the boundary. Then, the asymptotic network should look like that presented in figure 1. Clearly, the question of how to specify the network excitation, given arbitrary boundary conditions for the direct problem (3.1) in the continuum, is essential for the asymptotic theory to be applied in inversion. In this paper we address properly the issue of boundary conditions and show how to construct the asymptotic resistor network. We show that the peripheral nodes of the network are the points of intersection of the ridges of maximal conductivity with the boundary. Thus, the branches of the network as well as its interior and peripheral nodes are uniquely defined in terms of the conductivity function σ and they are independent of the boundary conditions in (1.1).

3.2. The asymptotic resistor network and its dual

In this section we establish the topology of the asymptotic resistor network and its dual. Then, in section 3.3, we define the DtN and NtD maps of the resistor network and show that they have variational formulations that are discrete equivalents of (2.4) and (2.9), respectively. Finally, in section 3.4, we show that the DtN and NtD maps of a high-contrast continuum (1.3) are asymptotically equivalent to the discrete DtN and NtD maps of the asymptotic resistor network.

Given any high-contrast conductivity function (1.3), the asymptotic resistor network has a topology uniquely defined by the ridges of maximal conductivity σ in Ω. The nodes of the network are the maxima of σ. Let us assume that $\sigma(\boldsymbol{x})$ has no critical point (minimum, maximum or saddle) along the boundary and extend the network to $\partial\Omega$ along ridges of maximal conductivity. Thus, the peripheral nodes of the network are at the intersection between the ridges of maximal conductivity and the boundary. The branches of the network connect the nodes through saddle points of σ. Finally, each branch carries a resistance given by (3.2). For the example considered in section 3.1, the resistor network is shown in figure 2 with the full line. Similarly, we introduce the dual network, uniquely defined by the ridges of minimal conductivity in Ω. The interior nodes of the dual network are the minima of σ in Ω. The peripheral nodes of the dual network are at the intersections between the ridges of minimal conductivity and the boundary. Finally, the branches of the network connect the nodes through saddle points of σ. The dual network for the example considered in section 3.1 is shown in figure 2 by the broken curves.

The construction illustrated in figure 2 is general and it allows us to define the direct and dual networks for any high-contrast function $\sigma(\boldsymbol{x})$. Suppose that the resistor network has a set $\mathcal{N}$ of nodes, where each node corresponds to a maximum of the function $\sigma(\boldsymbol{x})$. The set $\mathcal{N}$ is the union of the sets $\mathcal{N}_{\mathrm{I}}$ of internal nodes and $\mathcal{N}_{\mathrm{B}}$ of boundary nodes, such as a, b, c, d in figure 2. To each node $j \in \mathcal{N}$, we associate a potential Φ_j, where $\Phi_j = \Psi_j$ if $j \in \mathcal{N}_{\mathrm{B}}$. Let us consider the boundary node $j \in \mathcal{N}_{\mathrm{B}}$ located at s_j on $\partial\Omega$, where s is arc length along the boundary. We show in section 3.4 that the peripheral potential Ψ_j is given by

$$\Psi_j = \psi(s_j) \tag{3.3}$$

where ψ is the boundary voltage measured at the boundary of the high-contrast continuum. Next, suppose that the network has a set $\mathcal{M}$ of branches, where each branch accounts for a saddle of σ. Through the branch (j, k) that connects nodes j and k, we have the current J_{jk},

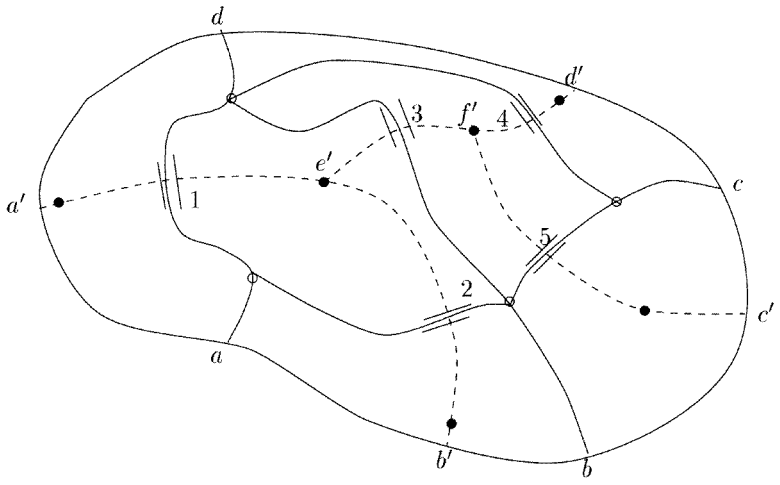

Figure 2. Direct and dual networks.

where

$$J_{jk} = -J_{kj} \qquad \text{for any } j \text{ and } k \in \mathcal{N}$$
$$\sum_{k\in\mathcal{V}_j} J_{jk} = \begin{cases} 0 & \text{if } j \in \mathcal{N}_I \\ \mathcal{I}_j & \text{if } j \in \mathcal{N}_{\mathrm{B}}. \end{cases} \tag{3.4}$$

In (3.4), $\mathcal{V}_j$ is the set of neighbours of $j \in \mathcal{N}$ and $\mathcal{I}_k$ is the excitation current at the boundary node $k \in \mathcal{N}_{\mathrm{B}}$. Consider a maximum $\boldsymbol{x}_k$ of σ, that is near the boundary. This maximum is directly connected to boundary node $k \in \mathcal{N}_{\mathrm{B}}$. We denote the closure of the basin of attraction of maximum $\boldsymbol{x}_k$ by $\overline{B}(\boldsymbol{x}_k)$. The intersection of $\overline{B}(\boldsymbol{x}_k)$ with $\partial\Omega$ gives the piece of boundary that lies between the dual boundary nodes that are adjacent to $k \in \mathcal{N}_{\mathrm{B}}$. We show in section 3.4 that $\boldsymbol{x}_k$ attracts all the current that penetrates through this piece of boundary or, equivalently,

$$\mathcal{I}_k = \int_{\partial\Omega \bigcap \overline{B}(\boldsymbol{x}_k)} I(\boldsymbol{x})\, \mathrm{d}s. \tag{3.5}$$

Similarly, the dual network has a set $\mathcal{N}'$ of nodes, where each node is associated with a minimum of σ. The set $\mathcal{N}'$ is given by the union of the set $\mathcal{N}'_{\mathrm{I}}$ of internal nodes and the set $\mathcal{N}'_{\mathrm{B}}$ of boundary nodes, such as nodes a', b', c' and d' in figure 2. The nodes of the dual network are connected by a set $\mathcal{M}'$ of branches, where each branch corresponds to a saddle point of the function σ. Evidently, the sets $\mathcal{M}$ and $\mathcal{M}'$ are identical. At each node $j' \in \mathcal{N}'$, we assign a potential $H_{j'}$, where $H_{j'} = h_{j'}$ if $j' \in \mathcal{N}'_{\mathrm{B}}$. Finally, to each branch (j', k') in $\mathcal{M}'$, we assign a current $F_{j'k'}$, where

$$F_{j'k'} = -F_{k'j'} \qquad \text{for any } j' \text{ and } k' \in \mathcal{N}'$$
$$\sum_{k'\in\mathcal{V}'_{j'}} F_{j'k'} = \begin{cases} 0 & \text{if } j' \in \mathcal{N}'_I \\ \mathcal{F}_{j'} & \text{if } j' \in \mathcal{N}'_{\mathrm{B}}. \end{cases} \tag{3.6}$$

In (3.6), $\mathcal{V}'_{j'}$ stands for the set of neighbours of $j' \in \mathcal{N}'$ and $\mathcal{F}_{k'}$ is the excitation current at the boundary node $k' \in \mathcal{N}'_{\mathrm{B}}$. The definition of $h_{j'}$ and $\mathcal{F}_{j'}$ for $j' \in \mathcal{N}'_{\mathrm{B}}$ is made precise in section 3.4.

In a two-dimensional continuum, any current $\boldsymbol{j}$ that satisfies $\nabla \cdot \boldsymbol{j} = 0$ can be written in terms of a stream function $H(\boldsymbol{x})$ as $\boldsymbol{j} = +(-\partial/\partial y, \partial/\partial x)H(\boldsymbol{x})$. Similarly, any network

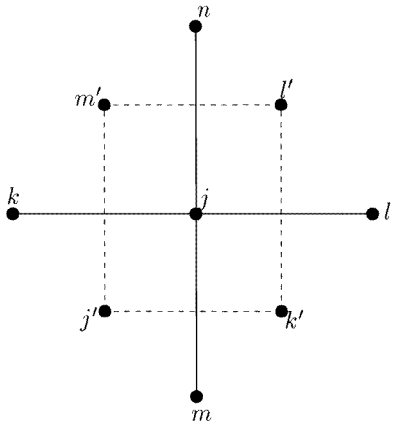

Figure 3. Node $j \in \mathcal{N}$ is surrounded by the loop j', k', l', m' in the dual network.

current distribution that obeys (3.4) can be written in terms of a potential defined at the nodes of the dual network. For example, consider the currents through the node $j \in \mathcal{N}$ shown in figure 3. They can be written as

$$J_{jk} = H_{m'} - H_{j'} \qquad J_{jl} = H_{k'} - H_{l'} \qquad J_{jn} = H_{l'} - H_{m'} \qquad J_{jm} = H_{j'} - H_{k'}. \quad (3.7)$$

Thus, the node law (3.4) is equivalent to a loop law for the potential differences in the dual network

$$\sum_{k \in \mathcal{V}_j} J_{jk} = \sum_{j\,\text{loop}} \Delta H = 0 \quad (3.8)$$

where we use the notation 'j loop' for the loop in the dual network that surrounds the node $j \in \mathcal{N}$. Likewise, the currents $F_{j'k'}$ in the dual network can be written as potential differences in the resistor network. This duality is a useful tool which we employ in the analysis given in sections 3.3 and 3.4.

3.3. The DtN and NtD maps of the asymptotic resistor network

We define the vectors of currents $\boldsymbol{\mathcal{I}} = (\mathcal{I}_1, \mathcal{I}_2, \ldots, \mathcal{I}_{N_B})^T$ and potentials $\boldsymbol{\Psi} = (\Psi_1, \Psi_2, \ldots, \Psi_{N_B})^T$, where N_B is the number of boundary nodes in the set $\mathcal{N}_B$ and the superscript T stands for transpose. The discrete DtN map $\Lambda^{D,\epsilon}$ is a symmetric $N_B \times N_B$ positive semidefinite matrix that gives the input/output current in terms of the boundary potential:

$$\mathcal{I}_j = \sum_{k \in \mathcal{N}_B} \Lambda^{D,\epsilon}_{jk} \Psi_k \qquad \text{for all } j \in \mathcal{N}_B. \quad (3.9)$$

The null space of the map $\Lambda^{D,\epsilon}$ is spanned by the vector $(1, 1, \ldots, 1)^T \in R^{N_B \times 1}$. The pseudoinverse of $\Lambda^{D,\epsilon}$ is the NtD map that gives the boundary potentials in terms of the currents:

$$\Psi_j = \sum_{k \in \mathcal{N}_B} (\Lambda^{D,\epsilon})^{-1}_{jk} \mathcal{I}_k \qquad \text{for all } j \in \mathcal{N}_B. \quad (3.10)$$

The domain of the map $(\Lambda^{D,\epsilon})^{-1}$ is the $(N_B - 1)$-dimensional space spanned by current vectors $\boldsymbol{\mathcal{I}} = (\mathcal{I}_1, \mathcal{I}_2, \ldots, \mathcal{I}_{N_B})^T \in R^{N_B \times 1}$ that satisfy the constraint

$$\sum_{j=1}^{N_B} \mathcal{I}_j = 0. \quad (3.11)$$

Finally, we define the quadratic forms

$$\langle \boldsymbol{\Psi}, \Lambda^{\mathrm{D},\epsilon}\boldsymbol{\Psi}\rangle = \sum_{j\in\mathcal{N}_{\mathrm{B}}} \mathcal{I}_j \Psi_j \qquad \langle \boldsymbol{\mathcal{I}}, (\Lambda^{\mathrm{D},\epsilon})^{-1}\boldsymbol{\mathcal{I}}\rangle = \sum_{j\in\mathcal{N}_{\mathrm{B}}} \mathcal{I}_j \Psi_j \tag{3.12}$$

for which we give the following lemma.

Lemma 1. *The quadratic forms (3.12) have the following variational formulations:*

$$\langle \boldsymbol{\Psi}, \Lambda^{\mathrm{D},\epsilon}\boldsymbol{\Psi}\rangle = \min_{\Phi_k=\Psi_k \text{ if } k\in\mathcal{N}_B} \frac{1}{2}\sum_{j\in\mathcal{N}}\sum_{k\in\mathcal{V}_j} \frac{1}{R^{\epsilon}_{jk}}(\Phi_j-\Phi_k)^2 \tag{3.13}$$

and

$$\langle \boldsymbol{\mathcal{I}}, (\Lambda^{\mathrm{D},\epsilon})^{-1}\boldsymbol{\mathcal{I}}\rangle = \min_{J_{jk} \text{ satisfy (3.4)}} \frac{1}{2}\sum_{j\in\mathcal{N}}\sum_{k\in\mathcal{V}_j} R^{\epsilon}_{jk} J^2_{jk}. \tag{3.14}$$

The resistance R^{ϵ}_{jk} in (3.13) and (3.14) is given by (3.2), where $\boldsymbol{x}_{\mathrm{s}}$ is the saddle point that connects the maxima $\boldsymbol{x}_j$ and $\boldsymbol{x}_k$ of σ or, equivalently, the nodes j and k in the network. The superscript ϵ reminds us that the resistance depends on the small parameter ϵ because of the factor $\sigma(\boldsymbol{x}_{\mathrm{s}}) = \sigma_0\, \mathrm{e}^{-S(\boldsymbol{x}_{\mathrm{s}})/\epsilon}$.

Proof of lemma 1. The equation that the minimizing currents J_{jk} in (3.14) must satisfy is

$$\sum_{j\in\mathcal{N}}\sum_{k\in\mathcal{V}_j} R^{\epsilon}_{jk} J_{jk}\delta J_{jk} = 0 \tag{3.15}$$

where δJ_{jk} is an arbitrary perturbation current distribution that satisfies

$$\sum_{k\in\mathcal{V}_j} \delta J_{jk} = 0 \qquad \text{for all } j\in\mathcal{N}. \tag{3.16}$$

As shown in section 3.2, such perturbation currents can be written in terms of a scalar potential $\delta H_{j'}$ defined at the nodes $j'\in\mathcal{N}'$ in the dual network

$$\delta J_{jk} = \delta H_{k'} - \delta H_{j'}. \tag{3.17}$$

In equation (3.17), the dual branch (j',k') corresponds to the same saddle point associated with the branch (j,k) in the resistor network. Then, (3.15) can be rewritten as

$$\sum_{j'\in\mathcal{N}'}\left[\sum_{k' \text{ loop}, k'\in\mathcal{V}'_{j'}} (R^{\epsilon}J)_{jk}\right]\delta H_{j'} = 0 \tag{3.18}$$

where we denote by k' loop the loop in the network that surrounds the dual node k'. Identity (3.18) is the analogue of integration by parts in a continuum and it says that the sum over the nodes in the resistor network can be replaced by a sum over loops of the products $R^{\epsilon}_{jk}J_{jk}$. The potentials $\delta H_{j'}$ are arbitrary so, for any loop in the resistor network, we must have

$$\sum_{k' \text{ loop}, k'\in\mathcal{V}'_{j'}} (R^{\epsilon}J)_{jk} = 0 \tag{3.19}$$

or, equivalently,

$$R^{\epsilon}_{jk}J_{jk} = \Phi_j - \Phi_k \tag{3.20}$$

where Φ_k is the scalar potential at node $k\in\mathcal{N}$. Equation (3.20) is easily recognized as Ohm's law. Equations (3.19) and (3.4) determine uniquely the minimizing current distribution J_{jk} for j and $k\in\mathcal{N}$. Furthermore, from (3.20) and (3.12) we have

$$\frac{1}{2}\sum_{j\in\mathcal{N}}\sum_{k\in\mathcal{V}_j} R^{\epsilon}_{jk}J^2_{jk} = \frac{1}{2}\sum_{j\in\mathcal{N}}\Phi_j\sum_{k\in\mathcal{N}} J_{jk} - \frac{1}{2}\sum_{k\in\mathcal{N}}\Phi_k\sum_{j\in\mathcal{N}} J_{jk} = \sum_{j\in\mathcal{N}_{\mathrm{B}}}\Psi_j\mathcal{I}_j = \langle \boldsymbol{\mathcal{I}}, (\Lambda^{\mathrm{D},\epsilon})^{-1}\boldsymbol{\mathcal{I}}\rangle. \tag{3.21}$$

Similarly, we obtain the variational principle (3.13) and the proof of lemma 1 is complete. □

3.4. Asymptotic limit of the DtN and NtD maps in high-contrast media

In this section we show that, in the limit $\epsilon \to 0$, or infinitely high contrast, the Dirichlet to Neumann map Λ^ϵ of a high-contrast continuum (1.3) is asymptotically equivalent to the discrete map $\Lambda^{\mathrm{D},\epsilon}$ of the resistor network. Similarly, we show that the Neumann to Dirichlet map, $(\Lambda^\epsilon)^{-1}$ is asymptotically equivalent to $(\Lambda^{\mathrm{D},\epsilon})^{-1}$. The proof relies on variational principles (2.4), (2.9), (3.13) and (3.14) and the method of matched asymptotic expansions.

Theorem 3.1. *Consider the asymptotic limit $\epsilon \to 0$. For any current $I(\boldsymbol{x}) \in H^{-1/2}(\partial\Omega)$ such that $\int_{\partial\Omega} I(\boldsymbol{x})\,\mathrm{d}s = 0$, we have the asymptotic equivalence:*

$$(I, (\Lambda^\epsilon)^{-1} I) = \langle \boldsymbol{\mathcal{I}}, (\Lambda^{\mathrm{D},\epsilon})^{-1} \boldsymbol{\mathcal{I}} \rangle [1 + o(1)]. \tag{3.22}$$

The components of $\boldsymbol{\mathcal{I}}$ are given by

$$\mathcal{I}_j = \int_{\partial\Omega \bigcap \overline{B}(\boldsymbol{x}_j)} I(\boldsymbol{x})\,\mathrm{d}s \tag{3.23}$$

where $\overline{B}(\boldsymbol{x}_j)$ is the closure of the basin of attraction of the maximum of σ associated with the boundary node $j \in \mathcal{N}_\mathrm{B}$. Furthermore, for any potential $\psi(\boldsymbol{x}) \in H^{1/2}(\partial\Omega)$, we have

$$(\psi, \Lambda^\epsilon \psi) = \langle \boldsymbol{\Psi}, \Lambda^{\mathrm{D},\epsilon} \boldsymbol{\Psi} \rangle [1 + o(1)]. \tag{3.24}$$

The components of $\boldsymbol{\Psi}$ are given by

$$\Psi_j = \psi(s_j) \tag{3.25}$$

where s_j denotes the point on $\partial\Omega$ that is associated with the boundary node $j \in \mathcal{N}_\mathrm{B}$. Recall from section 3.2 that points such as $s_j \in \partial\Omega$ are the intersections of ridges of maximal conductivity with the boundary.

The proof of theorem 3.1 has three main steps. In the first two steps, we calculate upper bounds on the quadratic forms $(\psi, \Lambda^\epsilon \psi)$ and $(I, (\Lambda^\epsilon)^{-1} I)$. In the third step, we use a duality argument to get lower bounds on $(\psi, \Lambda^\epsilon \psi)$ and $(I, (\Lambda^\epsilon)^{-1} I)$ that will match the upper bounds.

Lemma 2. *Given any current $I(\boldsymbol{x}) \in H^{-1/2}(\partial\Omega)$, we have the upper bound*

$$(I, (\Lambda^\epsilon)^{-1} I) \leqslant \langle \boldsymbol{\mathcal{I}}, (\Lambda^{\mathrm{D},\epsilon})^{-1} \boldsymbol{\mathcal{I}} \rangle [1 + o(1)].$$

Proof of lemma 2. To obtain an upper bound on $(I, (\Lambda^\epsilon)^{-1} I)$, we use the variational principle (2.9). We rewrite the current $\boldsymbol{j}$ as

$$\boldsymbol{j} = \nabla^\perp H \qquad \text{where } \nabla^\perp = \left(-\frac{\partial}{\partial y}, \frac{\partial}{\partial x} \right). \tag{3.26}$$

Then,

$$\nabla \cdot \boldsymbol{j} = 0 \text{ and } -\boldsymbol{j} \cdot \boldsymbol{n} = -\frac{\partial H}{\partial s} = I(s) \qquad \text{in } \partial\Omega \tag{3.27}$$

where s is the tangential coordinate at the boundary and $\boldsymbol{n}$ is the outer normal. Thus, the variational principle (2.9) becomes

$$(I, (\Lambda^\epsilon)^{-1} I) = \min_{H|_{\partial\Omega} = h} \int_\Omega \frac{1}{\sigma_0} \mathrm{e}^{S(\boldsymbol{x})/\epsilon} \nabla^\perp H(\boldsymbol{x}) \cdot \nabla^\perp H(\boldsymbol{x})\,\mathrm{d}\boldsymbol{x} \tag{3.28}$$

where

$$h(s) = -\int^s I(t)\,\mathrm{d}t. \tag{3.29}$$

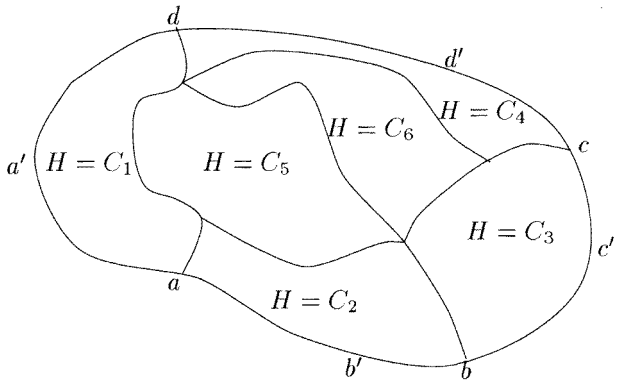

Figure 4. Trial field H for the upper bound on $(I, (\Lambda^\epsilon)^{-1} I)$. Away from the ridges of maximal conductivity, H is chosen constant. Across the ridges of maximal σ, H changes as given by (3.30).

In order to get an upper bound on $(I, (\Lambda^\epsilon)^{-1} I)$, we choose a trial field H. For simplicity, we start by assuming that the boundary excitation consists of localized current sources at the boundary nodes of the resistor network. Later on, we consider the case of general boundary conditions. From the asymptotic analysis in [10] and section 3.1, we know that the current $\boldsymbol{j}$ concentrates along the ridges of maximal conductivity or, equivalently, through the resistor network. Thus, we choose our trial field $H(\boldsymbol{x})$ to be a constant in vicinities of minima of σ that are delimited in the domain Ω by the flow line (resistor network). For the purpose of illustration, we show in figure 4 the trial field H chosen for the high-contrast $\sigma(\boldsymbol{x})$ considered in the example of section 3.1. The constant values of the trial field H at the boundary are completely determined by the current excitation, as shown by (3.29), whereas the ones in the interior are arbitrary so far. Across the ridges of maximal conductivity (full curve in figure 4), the trial field H changes as [10]

$$H(\boldsymbol{x}) = -\frac{f}{2}\operatorname{erf}\left(\frac{\eta}{\sqrt{2\epsilon/k(\xi)}}\right) + \text{ constant.} \tag{3.30}$$

In (3.30), f is the change of H across the flow line, (ξ, η) are coordinates defined along the flow line, where ξ is along the direction of the current (arc length), with $k(\xi)$ the local curvature of $S(x)$ in the η (normal) direction (see figure 5). The curvature k depends on the coordinate ξ and it is positive. Thus, in the vicinity of a ridge of maximal σ, we expand the scaled logarithm of the conductivity in a Taylor series

$$S(\boldsymbol{x}) = S(\xi, \eta) = g(\xi) + \frac{k(\xi)}{2}\eta^2 + \frac{1}{6}\frac{\partial^3 S}{\partial \eta^3}(\xi, 0)\eta^3 + \frac{1}{24}\frac{\partial^4 S}{\partial \eta^4}(\xi, 0)\eta^4 + \cdots \tag{3.31}$$

where $g(\xi) = S(\xi, 0)$ is a function of arc length along the ridge.

To calculate the trial current field $\boldsymbol{j}$ we take the perpendicular gradient in equation (3.30). Consider a point $\boldsymbol{x}(\xi)$ along a ridge of maximal conductivity, as shown in figure 5, and let $\dot{\boldsymbol{x}}(\xi)$ denote the unit tangent to the ridge at $\boldsymbol{x}(\xi)$. The unit normal is given by $\boldsymbol{N}(\xi)$. From equation (3.30), we observe that $H(\xi, \eta)$ changes abruptly in a small vicinity of the ridge and it is constant elsewhere. Thus, locally, we have

$$\boldsymbol{x} = \boldsymbol{x}(\xi) + \eta \boldsymbol{N}(\xi) \tag{3.32}$$

where $|\eta| \leqslant \delta$ and $\delta \to 0$ such that $\delta^2/\epsilon \to \infty$ as $\epsilon \to 0$. From (3.32) we obtain that

$$\mathrm{d}\boldsymbol{x} = [\dot{\boldsymbol{x}}(\xi) + \eta \dot{\boldsymbol{N}}(\xi)]\,\mathrm{d}\xi + \boldsymbol{N}(\xi)\,\mathrm{d}\eta$$

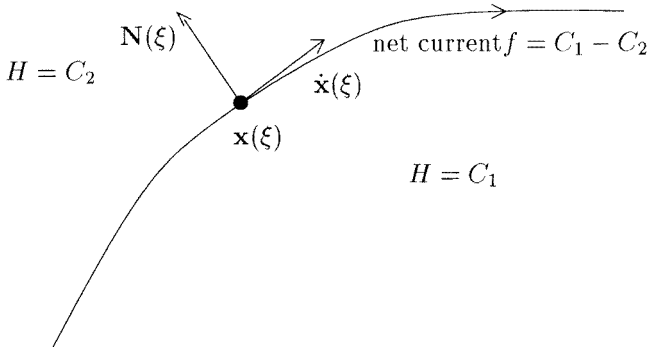

Figure 5. Local system of coordinates along the flow line.

or, since $\dot{\boldsymbol{N}}(\xi)$ is parallel to $\dot{\boldsymbol{x}}(\xi)$,

$$\mathrm{d}\boldsymbol{x} = [1 + \gamma(\xi)\eta]\dot{\boldsymbol{x}}(\xi)\,\mathrm{d}\xi + \boldsymbol{N}(\xi)\,\mathrm{d}\eta \qquad \text{where } \dot{\boldsymbol{N}}(\xi) = \gamma(\xi)\dot{\boldsymbol{x}}(\xi). \tag{3.33}$$

Therefore, the distance squared between two adjacent points near the ridge is

$$(\mathrm{d}s)^2 = \frac{1}{h_1^2}(\mathrm{d}\xi)^2 + \frac{1}{h_2^2}(\mathrm{d}\eta)^2 \qquad \text{where } h_1 = \frac{1}{1+\gamma(\xi)\eta} = 1 + O(\delta) \text{ and } h_2 = 1. \tag{3.34}$$

The trial current is obtained from (3.30) as

$$\boldsymbol{j} = -h_2\frac{\partial H}{\partial \eta}\dot{\boldsymbol{x}}(\xi) + h_1\frac{\partial H}{\partial \xi}\boldsymbol{N}(\xi)$$

or, equivalently,

$$\boldsymbol{j}(\boldsymbol{x}) = \frac{f}{\sqrt{2\pi\epsilon}}\,\mathrm{e}^{-k(\xi)\eta^2/2\epsilon}\left[\sqrt{k(\xi)}\hat{\xi} - \frac{\eta}{2\sqrt{k(\xi)}}\frac{\mathrm{d}k(\xi)}{\mathrm{d}\xi}(1 + O(\delta))\hat{\eta}\right] \tag{3.35}$$

where $\hat{\xi} = \dot{\boldsymbol{x}}(\xi)$ and $\hat{\eta} = \boldsymbol{N}(\xi)$ are the unit tangential and normal vectors, respectively. Thus, the trial current $\boldsymbol{j}$ is zero everywhere in Ω except in the vicinity of the ridges of maximal conductivity. Furthermore, the power dissipated is given by

$$\int_\Omega \frac{1}{\sigma(\boldsymbol{x})}|\boldsymbol{j}(\boldsymbol{x})|^2\,\mathrm{d}\boldsymbol{x} = \sum_{\text{tubes}}\int_{\text{tube}} \rho(\boldsymbol{x})|\boldsymbol{j}(\boldsymbol{x})|^2\,\mathrm{d}\boldsymbol{x} \tag{3.36}$$

where we sum over all the thin tubes around the ridges of maximal conductivity that confine the current $\boldsymbol{j}$.

Take any such tube that connects two nodes at the boundary through a couple of maxima and saddle points of $\sigma(\boldsymbol{x})$. For integration in the tube, $\mathrm{d}x\,\mathrm{d}y = (1/h_1h_2)\,\mathrm{d}\xi\,\mathrm{d}\eta = \mathrm{d}\xi\,\mathrm{d}\eta(1+O(\delta))$ and so

$$\int_{\text{tube}} \rho(\boldsymbol{x})|\boldsymbol{j}(\boldsymbol{x})|^2\,\mathrm{d}\boldsymbol{x} = \frac{1+O(\delta)}{2\pi\epsilon\sigma_0}\int_{\xi_{\text{in}}}^{\xi_{\text{out}}}\mathrm{d}\xi\int_{-\delta}^{\delta}\mathrm{d}\eta\,\mathrm{e}^{S(\xi,\eta)/\epsilon}[f(\xi)]^2$$
$$\times\mathrm{e}^{-k(\xi)\eta^2/\epsilon}\left[k(\xi) + \frac{\eta^2}{4k(\xi)}\left(\frac{\mathrm{d}k(\xi)}{\mathrm{d}\xi}\right)^2(1+O(\delta))\right]$$

where ξ_{in} and ξ_{out} are the boundary points and $\delta \ll 1$ is the width of the tube such that $\delta^2/\epsilon \to \infty$ as $\epsilon \to 0$. The net flux $f(\xi)$ through the tube is constant if there is no change of the tube, or it changes at the nodes of ramification. We use equation (3.1) for $S(\xi, \eta)$ and obtain

$$\int_{\text{tube}} \rho(\boldsymbol{x})|\boldsymbol{j}(\boldsymbol{x})|^2\,\mathrm{d}\boldsymbol{x} = \frac{1+O(\delta)}{2\pi\epsilon\sigma_0}\int_{\xi_{\text{in}}}^{\xi_{\text{out}}}[f(\xi)]^2\,\mathrm{e}^{g(\xi)/\epsilon}P(\xi) \tag{3.37}$$

where

$$P(\xi) = \int_{-\delta}^{\delta} \exp\left(-\frac{k(\xi)\eta^2}{2\epsilon} + \frac{1}{6\epsilon}\frac{\partial^3 S}{\partial \eta^3}(\xi,0)\eta^3 + \frac{1}{24\epsilon}\frac{\partial^4 S}{\partial \eta^4}(\xi,0)\eta^4 + \cdots \right) \times \left[k(\xi) + \frac{\eta^2}{4k(\xi)}\left(\frac{\mathrm{d}k(\xi)}{\mathrm{d}\xi}\right)^2 (1 + O(\delta)) \right] \mathrm{d}\eta. \tag{3.38}$$

With the change of coordinates $\eta = \sqrt{\epsilon}t$,

$$P(\xi) = \sqrt{\epsilon} \int_{-\delta/\sqrt{\epsilon}}^{\delta/\sqrt{\epsilon}} \mathrm{e}^{-\frac{1}{2}k(\xi)t^2}(1 + O(\sqrt{\epsilon}))\left[k(\xi) + \epsilon \frac{t^2}{4k(\xi)}\left(\frac{\mathrm{d}k(\xi)}{\mathrm{d}\xi}\right)^2 (1 + O(\delta)) \right] \mathrm{d}t \tag{3.39}$$

and, since $\delta \to 0$ such that $\delta/\sqrt{\epsilon} \to \infty$, as $\epsilon \to 0$,

$$P(\xi) = \sqrt{2\pi k(\xi)\epsilon}(1 + O(\sqrt{\epsilon})). \tag{3.40}$$

Thus, equation (3.37) becomes

$$\int_{\text{tube}} \rho(\boldsymbol{x})|\boldsymbol{j}(\boldsymbol{x})|^2 \,\mathrm{d}\boldsymbol{x} = \frac{1 + O(\delta)}{\sigma_0} \int_{\xi_{\text{in}}}^{\xi_{\text{out}}} \sqrt{\frac{k(\xi)}{2\pi\epsilon}} [f(\xi)]^2 \,\mathrm{e}^{g(\xi)/\epsilon} \,\mathrm{d}\xi. \tag{3.41}$$

The integral (3.41) is of Laplace type [4], and the main contribution comes from the maxima of $g(\xi)$. However, the only maxima of $g(\xi)$ along the tube are the saddle points of σ. Consider a saddle point $\boldsymbol{x}_{\text{s}} = (\xi_{\text{s}}, 0)$ along the tube. In the vicinity of ξ_{s}, $g(\xi)$ is given by

$$g(\xi) = S(\boldsymbol{x}_{\text{s}}) - \frac{p(\boldsymbol{x}_{\text{s}})(\xi - \xi_{\text{s}})^2}{2} + \frac{(\xi - \xi_{\text{s}})^3}{6}\frac{\partial^3 g}{\partial \xi^3}(\xi_{\text{s}}) + \cdots \tag{3.42}$$

where $p(\boldsymbol{x}_{\text{s}}) > 0$ is the curvature of function S at the saddle point, in the direction $\hat{\xi}$. Hence, the contribution of this saddle point to the integral in (3.41) is

$$\frac{(1 + O(\delta))}{\sigma_0} \int_{\xi - \xi_{\text{s}}}^{\xi + \xi_{\text{s}}} \exp\left(\frac{S(\boldsymbol{x}_{\text{s}})}{\epsilon} - \frac{p(\boldsymbol{x}_s)(\xi - \xi_s)^2}{2\epsilon} + \frac{(\xi - \xi_s)^3}{6\epsilon}\frac{\partial^3 g}{\partial \xi^3}(\xi_s) + \cdots \right) \times \sqrt{\frac{k(\xi)}{2\pi\epsilon}} [f(\xi)]^2 \,\mathrm{d}\xi = \frac{[f(\boldsymbol{x}_{\text{s}})]^2}{\sigma(\boldsymbol{x}_{\text{s}})} \sqrt{\frac{k(\boldsymbol{x}_{\text{s}})}{p(\boldsymbol{x}_{\text{s}})}}(1 + O(\delta)).$$

Finally, we add the contribution of all saddle points along the tube and, since $\delta \ll 1$, we obtain

$$\int_{\text{tube}} \rho(\boldsymbol{x})|\boldsymbol{j}(\boldsymbol{x})|^2 \,\mathrm{d}\boldsymbol{x} = \sum_{\boldsymbol{x}_{\text{s}}} [f(\boldsymbol{x}_{\text{s}})]^2 R(\boldsymbol{x}_{\text{s}})(1 + o(1)) \tag{3.43}$$

where $R(\boldsymbol{x}_{\text{s}}) = (1/\sigma(\boldsymbol{x}_{\text{s}}))\sqrt{k(\boldsymbol{x}_{\text{s}})/p(\boldsymbol{x}_{\text{s}})}$ is the resistance associated with the saddle $\boldsymbol{x}_{\text{s}}$.

Clearly, the same calculation applies to all branches or ridges of maximal conductivity in the domain Ω. Next, consider the basin of attraction of a maximum $\boldsymbol{x}_j$ of σ that is near the boundary. For example, consider figure 2, where $\boldsymbol{x}_j$ is the maximum associated with the node a in the resistor network. This maximum has a basin of attraction that is delimited from the rest of the domain by the broken curve that goes through the nodes a', e' and b' of the dual network. Across this line, we have two channels of strong flow, at saddles 1 and 2. Suppose that we have the fluxes f_1 and f_2 through saddles 1 and 2, respectively. However, the current is given by $\nabla^{\perp} H$, so the total current across the broken curve $a'e'b'$ must satisfy

$$f_1 + f_2 = \int_{a'e'b'} -\frac{\partial H}{\partial s} \,\mathrm{d}s = h_{b'} - h_{a'} \tag{3.44}$$

where s is the coordinate along the curve $a'e'b'$. Finally, from (3.29) we have that

$$f_1 + f_2 = \int_{\partial\Omega \bigcap \overline{B}(\boldsymbol{x}_{\text{a}})} I(\boldsymbol{x}) \,\mathrm{d}s = \mathcal{I}_{\text{a}} \tag{3.45}$$

where $\mathcal{I}_a$ is the total current penetrating the piece of boundary that falls into the basin of attraction of the maximum $\boldsymbol{x}_j$ of σ. Clearly, this argument can be extended to any high-contrast $\sigma(\boldsymbol{x})$ and the conclusion is that the fluxes f must satisfy (3.4) or, equivalently, they must satisfy Kirchhoff's node law for currents. Next, we use the notation of section 3.2 and rewrite the sum in (3.43) as a sum over nodes in the asymptotic resistor network. Finally, from (3.28), (3.43) and lemma 1, we have the upper bound

$$(I, (\Lambda^\epsilon)^{-1} I) \leqslant (1 + o(1)) \min_{f_{jk} \text{ satisfy (3.4)}} \frac{1}{2} \sum_{j \in \mathcal{N}} \sum_{k \in \mathcal{V}_j} R^\epsilon_{jk} f^2_{jk} = \langle \boldsymbol{\mathcal{I}}, (\Lambda^{\mathrm{D},\epsilon})^{-1} \boldsymbol{\mathcal{I}} \rangle (1 + o(1)). \tag{3.46}$$

To complete the proof of lemma 2, we show that (3.46) holds for any current excitation I and not just for currents concentrated at boundary nodes, such as a, b, c and d in figure 2. In the case of a general current excitation I at $\partial\Omega$, the boundary potential h defined in (3.29) is not constant between two adjacent boundary nodes. Then, near the boundary, in a layer of width $\delta \ll 1$ chosen such that $\delta^2/\epsilon \to \infty$ as $\epsilon \to 0$, we extend the boundary potential h to the desired form given by (3.30) inside Ω. This is done in appendix A, where we show that the power dissipated in the layer is of the order ϵ/δ^2 and so it is negligible with respect to the power dissipated at the saddle points of σ, in the interior of the domain of the solution. The proof of lemma 2 is now complete. □

Likewise, for the quadratic form $(\psi, \Lambda^\epsilon \psi)$, we have the following result.

Lemma 3. *Given any boundary potential $\psi(\boldsymbol{x}) \in H^{1/2}(\partial\Omega)$, we have the upper bound*

$$(\psi, \Lambda^\epsilon \psi) \leqslant \langle \boldsymbol{\Psi}, \Lambda^{\mathrm{D},\epsilon} \boldsymbol{\Psi} \rangle (1 + o(1)).$$

Proof of lemma 3. To obtain an upper bound on $(\psi, \Lambda^\epsilon \psi)$, we use the variational principle (2.4). At the boundary, we define the dual current

$$F(s) = \nabla^\perp \phi(s) \cdot \boldsymbol{n} = -\frac{\mathrm{d}\psi}{\mathrm{d}s} \tag{3.47}$$

where s is the coordinate along $\partial\Omega$ and $\boldsymbol{n}$ is the outer normal. The variational principle (2.4) is rewritten in the form

$$(\psi, \Lambda^\epsilon \psi) = \min_{\nabla^\perp \phi \cdot \boldsymbol{n}|_{\partial\Omega} = F} \int_\Omega \sigma_0 \, \mathrm{e}^{-S(\boldsymbol{x})/\epsilon} \nabla^\perp \phi(\boldsymbol{x}) \cdot \nabla^\perp \phi(\boldsymbol{x}) \, \mathrm{d}\boldsymbol{x} \tag{3.48}$$

which is similar to (2.9). Hence, the proof of lemma 3 is almost identical to the proof of lemma 2. The only difference is that instead of looking at ridges of maximal conductivity (resistor network), we look at ridges of minimal σ (dual network). The result is

$$(\psi, \Lambda^\epsilon \psi) \leqslant (1 + o(1)) \min_{F_{j'k'}} \frac{1}{2} \sum_{j' \in \mathcal{N}'} \sum_{k' \in \mathcal{V}'_j} \frac{1}{R^\epsilon_{j'k'}} F^2_{j'k'} \tag{3.49}$$

where we sum over the nodes of the dual network and $F_{j'k'}$ is the dual current in the dual branch (j', k'). The eligible dual currents $F_{j'k'}$ in (3.49) satisfy (3.6). Similar to the vector $\boldsymbol{\mathcal{I}}$ of excitation currents in the resistor network, $\boldsymbol{\mathcal{F}}$ has N'_B components, where the component $\mathcal{F}_{j'}$ corresponds to the dual boundary node $j' \in \mathcal{N}'_B$. However, j' is associated with a minimum $\boldsymbol{x}_{j'}$ of σ, located near $\partial\Omega$. Thus, $\mathcal{F}'_j$ is the net dual current that penetrates the piece of the boundary belonging to the basin of attraction of the minimum $\boldsymbol{x}_{j'}$. For simplicity of explanation, we refer again to the example in figure 2. Consider the minimum of σ that corresponds to the dual

node a'. The basin of attraction of this minimum is delimited by the full curve $a1d$, which is a ridge of maximal conductivity. Then, the component of $\boldsymbol{\mathcal{F}}$ that corresponds to node a' is

$$\mathcal{F}_{a'} = \int_{\partial\Omega \bigcap \overline{B}(a')} F(s)\,\mathrm{d}s = \int_{\partial\Omega \bigcap \overline{B}(a')} -\frac{\mathrm{d}\psi}{\mathrm{d}s}\,\mathrm{d}s = \psi(a) - \psi(d). \tag{3.50}$$

Thus, the dual current $\mathcal{F}_{a'}$ is given by the potential drop between the nodes a and d in the resistor network, where $\Psi_a = \psi(a)$ and $\Psi_d = \psi(d)$. The argument holds for any minimum of the conductivity, located near $\partial\Omega$. In conclusion, the components of $\mathcal{F}$ are given by potential differences between the boundary nodes of the asymptotic resistor network and, from (3.13) and (3.49), we have the upper bound

$$(\psi, \Lambda^{\epsilon}\psi) \leqslant \langle \boldsymbol{\Psi}, \Lambda^{\mathrm{D},\epsilon}\boldsymbol{\Psi}\rangle(1 + o(1)). \tag{3.51}$$

Lemma 3 is now proved. □

Proof of theorem 3.1. We begin with the duality relation

$$(\psi, \Lambda^{\epsilon}\psi) = \sup_{I \in H^{-1/2}(\partial\Omega)} [2(I, \psi) - (I, (\Lambda^{\epsilon})^{-1}I)]. \tag{3.52}$$

To obtain a lower bound for $(\psi, \Lambda^{\epsilon}\psi)$, we take the trial field

$$I(s) = \sum_{j \in \mathcal{N}_{\mathrm{B}}} \frac{\mathcal{I}_j}{\sqrt{2\pi\delta}}\,\mathrm{e}^{-(s-s_j)^2/2\delta} \tag{3.53}$$

where δ is a small parameter and s is the coordinate along the boundary. Then,

$$(I, \psi) = \sum_{j \in \mathcal{N}_{\mathrm{B}}} \mathcal{I}_j \int_{\partial\Omega} \frac{\psi(s)}{\sqrt{2\pi\delta}}\,\mathrm{e}^{-(s-s_j)^2/2\delta}\,\mathrm{d}s = \sum_{j \in \mathcal{N}_{\mathrm{B}}} \mathcal{I}_j \Psi_j (1 + O(\delta)) \tag{3.54}$$

and, from lemma 2, (3.52) and (3.54), we have

$$(\psi, \Lambda^{\epsilon}\psi) \geqslant (1 + o(1)) \sup_{\mathcal{I}} [2\langle \boldsymbol{\Psi}, \boldsymbol{\mathcal{I}}\rangle - \langle \boldsymbol{\mathcal{I}}, (\Lambda^{\mathrm{D},\epsilon})^{-1}\boldsymbol{\mathcal{I}}\rangle] = \langle \boldsymbol{\Psi}, \Lambda^{\mathrm{D},\epsilon}\boldsymbol{\Psi}\rangle(1 + o(1)). \tag{3.55}$$

But, the lower bound (3.55) matches the upper bound given in lemma 3 and so

$$(\psi, \Lambda^{\epsilon}\psi) = \langle \boldsymbol{\Psi}, \Lambda^{\mathrm{D},\epsilon}\boldsymbol{\Psi}\rangle(1 + o(1)). \tag{3.56}$$

The proof of theorem 3.1 is completed with the observation that (3.56) implies

$$(I, (\Lambda^{\epsilon})^{-1}I) = \langle \boldsymbol{\mathcal{I}}, (\Lambda^{\mathrm{D},\epsilon})^{-1}\boldsymbol{\mathcal{I}}\rangle(1 + o(1)) \tag{3.57}$$

as well. □

3.5. Summary of the asymptotic analysis

The results of this section show that, for a high-contrast conductivity (1.3), the DtN and NtD maps given by (2.1) and (2.5), respectively, are asymptotically equivalent to the maps (3.9) and (3.10) of the asymptotic resistor network. The asymptotic network is uniquely determined by the critical points (maxima and saddle points) of the conductivity, in the domain Ω of the solution. Since in inversion, our data is the NtD or DtN map, imaging σ given by (1.3) is asymptotically equivalent to the identification of a resistor network from measurements of currents and voltages at the peripheral nodes. Furthermore, in high-contrast inversion, the most important features of the conductivity are the saddle points. Each saddle point of σ is equivalent to a resistor in the asymptotic network and brings a significant contribution to quadratic forms (2.4) and (2.9) or, equivalently, to the eigenvalues of the DtN and NtD maps.

The location of maxima and minima of σ in Ω determine the current flow topology and so they influence the spectra of the DtN and NtD maps. However, the actual value of σ at the maxima and minima is not important in the asymptotic limit. Therefore, when imaging a high-contrast conductivity (1.3), we cannot expect a good estimate of the value of σ at the minima or maxima. We should get, however, a good image at the saddle points as well as a fair localization of all critical points.

The question of unique recovery of resistor networks from the discrete DtN or NtD maps has been considered in [14, 15, 18]. It is shown that, in theory, rectangular resistor networks can be uniquely recovered. Furthermore, more general resistor networks can be uniquely recovered up to $Y-\Delta$ transformations (see [15] for details). However, the question of how to image these networks in practice does not have a satisfactory answer, so far. In the next section, we propose imaging asymptotic resistor networks with the method of matching pursuit [32]. We show that matching pursuit is effective in imaging high-contrast conductive media if the library of functions is carefully constructed to capture the features of σ that are essential in the asymptotic theory.

4. High-contrast inversion

In practice, we cannot expect the conductivity to be exactly like model (1.3). A more realistic conductivity has a few high-contrast peaks and valleys in a background of smaller scale variations. Hence, even though σ might have many saddle points, maxima and minima, only a few of these critical points dominate. Equivalently, we can view our domain as consisting of a few regions $\mathcal{D}_j$, $j = 1, \ldots, m$, where the contrast is high and the conductivity can be reasonably modelled by (1.3). In these high-contrast regions, the current flow is strongly channelled and the asymptotic resistor network approximation of section 3 and [10] holds. Elsewhere in the domain, the variations of σ are on a much smaller scale and the flow is diffuse. Thus, in a first step of inversion, the small changes of σ that occur in $\Omega \setminus \bigcup_{j=1}^{m} \mathcal{D}_j$ can be neglected in comparison to the high-contrast variations in $\bigcup_{j=1}^{m} \mathcal{D}_j$. Equivalently, the conducting material in Ω can be modelled as a constant background of conductivity σ_b in which we embed 'islands' $\mathcal{D}_j$, $j = 1, \ldots, m$ of high-contrast variation. This has been proposed in [9], where, in the first step of inversion, σ is parametrized as

$$\sigma(\boldsymbol{x}) \sim \tilde{\sigma}(\boldsymbol{x}; \boldsymbol{s}_1, \ldots, \boldsymbol{s}_m) = \sigma_{\mathrm{b}} + \sum_{j=1}^{m} \chi_j(\boldsymbol{x}, \boldsymbol{s}_j) f_j(\boldsymbol{x}, \boldsymbol{s}_j) \tag{4.1}$$

where $f_j(\cdot)$ are high-contrast modules embedded in the background σ_{b}. Each high-contrast module is chosen, in agreement with the asymptotic theory, as $f_j \sim \mathrm{e}^{-S/\epsilon}$, with support in Ω and it consists of a saddle point surrounded by two maxima and two minima. The structure of f_j is described through a vector of parameters $\boldsymbol{s}_j$ such as the position of the saddle points, orientation, etc. The modules f_j are localized with the smooth cut-off functions χ_j. The first step of the high-contrast imaging problem is: find σ_{b} and the set of parameters $\boldsymbol{s}_j$, $j = 1, \ldots, m$, given partial knowledge of the NtD map. The image $\tilde{\sigma}$ is in general a crude estimate of σ. However, as shown in section 3 and [9, 10], $\tilde{\sigma}$ gives a good approximation of current $\boldsymbol{j}(\boldsymbol{x})$ and voltage $\phi(\boldsymbol{x})$ in Ω. To improve the image, we can do a second step of inversion, based on linearization of (1.1) about the reference conductivity $\tilde{\sigma}$. In [9] we illustrate both steps of inversion. In this section, we concentrate on finding $\tilde{\sigma}$ given by (4.1). Specifically, we use the method of matching pursuit, for various choices of the high-contrast modules f_j.

4.1. Model of the logarithm of the conductivity as a product of sine functions

In [9] we model the high-contrast modules as

$$f(\boldsymbol{x}, \boldsymbol{s}) = \sigma_0 \exp\left\{\frac{1}{\epsilon}\sin[\alpha((x - x_s)\cos\theta + (y - y_s)\sin\theta)]\right.$$
$$\left.\times \sin[\beta((y - y_s)\cos\theta - (x - x_s)\sin\theta)]\right\} \tag{4.2}$$

where (x_s, y_s) is the location of the saddle point of the conductivity, θ is the orientation of the saddle and ϵ determines the contrast. The function $f(\cdot)$ in (4.2) is periodic with periods determined by α and β, which also determine the curvatures at the saddle. The constant σ_0 controls the height of the saddle. Thus, the high-contrast conductivity module is completely described by the seven-component vector

$$\boldsymbol{s} = (\sigma_0, \alpha, \beta, x_s, y_s, \theta, \epsilon). \tag{4.3}$$

The high-contrast module $f(\cdot)$ is tapered with the C^1 cutoff function

$$\chi(\boldsymbol{x}, \boldsymbol{s}) = g[(x - x_s)\cos\theta + (y - y_s), \alpha]g[-(x - x_s)\sin\theta + (y - y_s)\cos\theta), \beta] \tag{4.4}$$

where

$$g(\xi, \gamma) = \begin{cases} \sin^3\left[\dfrac{\pi}{2}\left(\xi + \dfrac{\pi}{\gamma}\right)\Big/ d\right] & \text{for } -\dfrac{\pi}{\gamma} \leqslant \xi \leqslant -\dfrac{\pi}{\gamma} + d \\ -\sin^3\left[\dfrac{\pi}{2}\left(\xi - \dfrac{\pi}{\gamma}\right)\Big/ d\right] & \text{for } \dfrac{\pi}{\gamma} - d \leqslant \xi \leqslant \dfrac{\pi}{\gamma} \\ 1 & \text{for } -\dfrac{\pi}{\gamma} + d \leqslant \dfrac{\pi}{\gamma} - d \\ 0 & \text{for } |\xi| \geqslant \dfrac{\pi}{\gamma}. \end{cases} \tag{4.5}$$

The parameter d in (4.5) controls the sharpness of the cutoff and it is kept constant throughout the numerical experiments. The inversion procedure with the choice (4.2) is discussed in detail in [9] and numerical experiments are also presented. It is clear that there are many possible choices one can make for the high-contrast modules f_j in (4.1); the choice (4.2) is just one of many. The question is how can we find an *optimal* model for f_j in some sense. The model ideally depends on what we expect σ to look like; it should depend on as few parameters as possible but it should be flexible enough to allow a reasonable representation of the high-contrast features of σ. In the next section we introduce another model for $f_j(\cdot)$ that depends on only two extra parameters but it is much more flexible than (4.2) and it permits better images to be obtained.

4.2. Cubic model of the logarithm of the conductivity

Choice (4.2) of high-contrast modules f_j allows for translation in Ω, scaling and different orientations of the channel. However, (4.2) is not general enough to allow different heights of the maxima or different depths of the minima surrounding the channel developed at the saddle point of $\sigma(\boldsymbol{x})$. A better choice is

$$f_j(\boldsymbol{s}_j, x, y) = \sigma_j \exp(S(x, y)/\epsilon_j) \tag{4.6}$$

where

$$S(x, y) = \alpha_j \xi(\beta_j + \alpha_j \xi)(1 - \beta_j - \alpha_j \xi)\gamma_j \eta(\delta_j + \gamma_j \eta)(1 - \delta_j - \gamma_j \eta)$$
$$\xi = (x - x_j)\cos\theta_j + (y - y_j)\sin\theta_j$$
$$\eta = -(x - x_j)\sin\theta_j + (y - y_j)\cos\theta_j \tag{4.7}$$

and

$$\boldsymbol{s}_j = (\sigma_j, \epsilon_j, \alpha_j, \beta_j, \gamma_j, \delta_j, x_j, y_j, \theta_j). \tag{4.8}$$

We localize the high-contrast module $f_j(\cdot)$ given by (4.6) over a period

$$(\xi, \eta) \in \left[-\frac{\beta_j}{\alpha_j}, \frac{1 - \beta_j}{\alpha_j} \right] \left[\frac{\delta_j}{\gamma_j}, \frac{1 - \delta_j}{\gamma_j} \right] = P_j \subset \Omega$$

with the cutoff function χ given by (4.5). Over a period $P_j \subset \Omega$, $f_j(\cdot)$ given by (4.6) has a saddle point at (x_j, y_j) with orientation θ_j, conductivity σ_j and contrast determined by the parameter ϵ_j. Parameters α_j and γ_j give the scaling of f_j and, by varying β_j and δ_j, we can obtain different heights or depths of the maxima or minima of f_j.

5. Matching pursuit with the high-contrast library

In this section we describe numerical experiments that demonstrate the performance and efficiency of the high-contrast library described in section 4.2. The identification of the optimal set of parameters $\{\boldsymbol{s}_j\}$, $j = 1, \ldots, m$ given by (4.8) is done with an output least-squares approach. Thus, we minimize the error in the electric potential at the boundary

$$E(\boldsymbol{s}_1, \ldots, \boldsymbol{s}_m) = \sum_{i=1}^{M} \sum_{k=1}^{N} [\psi_k^{(i)} - \phi_k^{(i)}(\boldsymbol{s}_1, \ldots, \boldsymbol{s}_m)]^2 \tag{5.1}$$

where $\psi_k^{(i)}$ is the electric potential measured at the kth electrode for a particular choice of the current excitation denoted by the superscript (i). The electric potential predicted at the boundary by the current guess of the conductivity is given by $\phi_k^{(i)}$, where the subscripts k and superscripts (i) have the same meaning as explained above. Thus, for a given guess $\tilde{\sigma}(\boldsymbol{x}; \boldsymbol{s}_1, \ldots, \boldsymbol{s}_m)$ of the conductivity and a current excitation $I^{(i)}(\boldsymbol{x})$ at the boundary, we calculate the potential $\phi^{(i)}(\boldsymbol{x})$ by solving equation (1.1). We use the software package PLTMG [3], which solves two-dimensional elliptic partial differential equations with a multigrid approach, on an adaptive triangulation of Ω. We also use Tikhonov regularization in our least squares, as explained in appendix B.

The task of our numerical calculations in this section is to find the conductivity $\tilde{\sigma}$, modelled by (4.1), that best fits the data. An important question that arises right from the start is: how many high-contrast modules should we have in (4.1). This is a difficult question for which we do not have an optimal answer. Our attempt to address the issue of multiple high-contrast modules uses the method of matching pursuit, where we search for one module at a time. In [7] we use this approach to image media with less than three high-contrast modules. Thus, we start our search with a single high-contrast module $f_1(\boldsymbol{x}, \boldsymbol{s}_1)$ embedded in the background σ_b. We find the optimal set of parameters $\boldsymbol{s}_1$ that minimizes the squared residual at the boundary (see figure 9). During this process, the residual decreases continually, until it reaches a plateau. When this plateau is reached, we conclude that we have found the first module. Then, we search for a second module $f_2(\boldsymbol{x}, \boldsymbol{s}_2)$, while the location and orientation of module f_1 is kept fixed. However, we do allow the magnitude of the conductivity of module f_1 to change. Again, we watch the evolution of the squared residual at the boundary. The residual increases initially, due to the insertion of the second module, but then it decreases continually, until it

reaches a second plateau. At this point, we conclude that we have found the second high-contrast module. We continue this procedure and stop when the residual at the boundary does not decrease anymore. This approach worked well in our numerical experiments in [7]. We find satisfactory images of high-contrast conductivities with up to three high-contrast channels (saddles of σ) provided that they are sufficiently well separated. If the channels are too close to each other, the algorithm tries to fit the modules f_i in between. This is a well known fault of the method of matching pursuit. However, when the channels are sufficiently far apart, our numerical experiments [7] are successful. It is worth mentioning that the philosophy of basing our imaging algorithm entirely on the decrease of the squared residual at the boundary, may be faulty. Indeed, we could imagine that by adding more and more parameters to our model we could reduce the residual to an arbitrary small value. Thus, a more sophisticated approach that penalizes too many parameters could be used [1, 36]. Note, however, that in our numerical experiments [7] we did not notice this phenomenon. Indeed, for a high-contrast σ with three channels that are well separated, we find a good approximation of the conductivity with three modules f_1, f_2 and f_3. Then, we insert in our search a fourth module, f_4. Depending on the initial location of f_4, this module either merges with one of the other three f_i or it is suppressed to zero. Hence, in our experiments we notice surprising stability with respect to the number of high-contrast channels. However, this may not be true for very noisy data, where a trade off between model complexity and data fit [1, 36] may be more appropriate.

The cubic model (4.6) for f_j that we use in our computations is more general than the model (4.2) considered in [9] at the expense of only two extra parameters. However, the additional flexibility of the model is reflected in a decrease of stability of the numerical process of recovering the optimal $\boldsymbol{s}_j$ from the boundary data. The inversion process can be easily stabilized as follows. From the results presented in [9] and the asymptotic theory developed in [10] and section 3, we know that, among the nine components of $\boldsymbol{s}_j$, the controlling ones are the location of the saddle point and its orientation. After x_j, y_j and θ_j have been successfully approximated, the rest of the parameters are easily recovered. If we search for all nine components at once, the inversion process can break down. Before finding the right location of the channel, the algorithm can give very poor values of β_j and δ_j that can even lead to the complete disappearance of one peak (maximum) and destroy the saddle structure that is essential for the identification of a channel in Ω. Hence, in all our numerical calculations, to identify the optimal set of parameters $\boldsymbol{s}_j = (\sigma_j, \epsilon_j, \alpha_j, \beta_j, \gamma_j, \delta_j, x_j, y_j, \theta_j)$, we proceed as follows. We choose an initial guess of $\boldsymbol{s}_j$ and we fix $\sigma_j, \epsilon_j, \alpha_j, \beta_j, \gamma_j$ and δ_j. The choice of these parameters proves not to be important in imaging f_j, as long as σ_j and ϵ_j do not give a contrast that is too high for the numerical solver PLTMG to calculate an accurate solution of (1.1). Furthermore, α_j and β_j should be chosen such that the support of f_j lies in the interior of Ω. Finally, β_j and δ_j should be chosen such that f_j has a structure of two maxima, two minima and a saddle in between. A reckless choice of these parameters could suppress one peak of f_j and thus destroy the saddle point which is the essential feature in high-contrast inversion. Then we search for parameters x_j, y_j and θ_j that minimize the residual squared at the boundary. After we find them, we allow all parameters in $\boldsymbol{s}_j$ to change in our search of the optimal high-contrast module $f(\boldsymbol{x}, \boldsymbol{s}_j)$.

All numerical experiments presented in this section use numerically generated data to which we add noise in some cases. We assume that the electric potential is given at 32 uniformly distributed points along three of the straight boundaries of a square domain. Furthermore, we have six different patterns of current excitation corresponding to different locations of the current source and sink, respectively. The high-contrast experiments presented in section 4.1 could have been done with as few as two different current excitations. However, for the intermediate case considered in section 4.2, more data were needed so, for consistency, we use the same data for all the experiments presented in this paper.

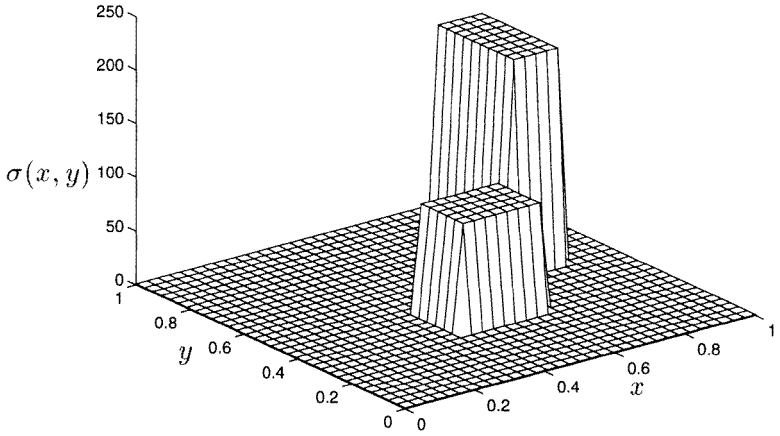

Figure 6. High-contrast model conductivity with square inclusions.

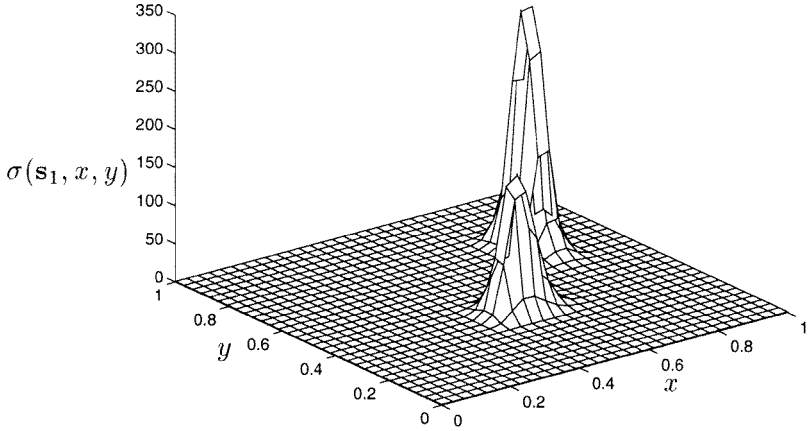

Figure 7. Reconstructed conductivity with high-contrast model (4.6).

5.1. High-contrast imaging

The first numerical experiment illustrates the imaging of a high-contrast medium with two square-shaped conducting inclusions embedded in a background $\sigma_b = 1$. The conductivity of one inclusion is $\sigma_1 = 100$ and the other inclusion has conductivity $\sigma_2 = 200$. The model conductivity that we want to image is shown in figure 6. The result of the inversion with a conductivity consisting of a uniform background and a high-contrast module given by (4.6) is shown in figure 7. It is clear that since we limit our search to a specific class of smooth functions we cannot obtain very good quantitative results of the image of σ. Furthermore, the asymptotic theory (see section 3 and [10]) shows that near the peaks of the conductivity, the potential gradient $\nabla\phi$ is nearly zero. Thus, there is little information about the conductivity at the local maxima and we cannot expect a good image there. However, the result we have is still very informative. Even though the magnitude of the conductivity at the peaks does not coincide with the conductivity of the inclusions, the result localizes the inclusions very well (see figure 8) and does indicate correctly which inclusion has the highest conductivity. Moreover, the ratio of two between the conductivity of the two inclusions is estimated correctly in the

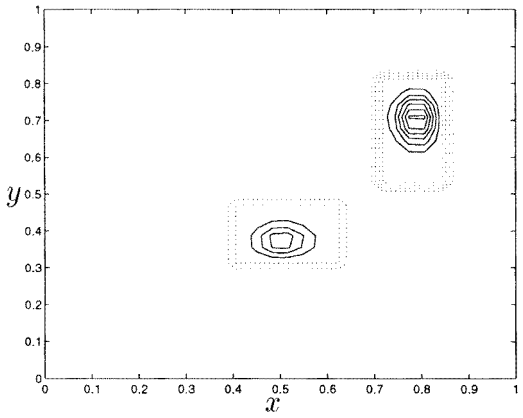

Figure 8. Contour plot of model conductivity (dotted curve) and reconstructed conductivity with high-contrast model (4.6) (full curve).

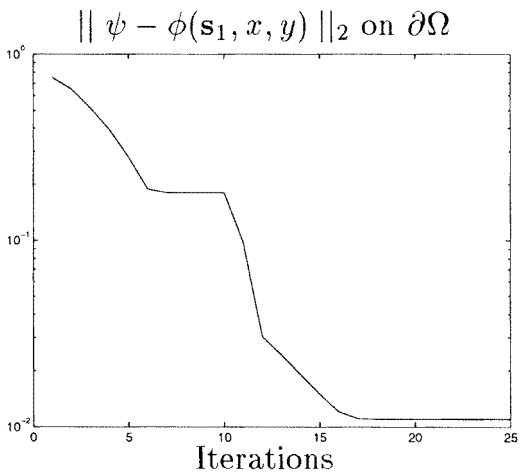

Figure 9. Evolution of the error in the potential at the boundary.

image, where $\sigma_2/\sigma_1 = 1.9576$. The plot of the error in the electric potential at the boundary is shown in figure 9. Note that the inversion is done, as discussed before, by searching first for the location and orientation of the channel while all other parameters are kept fixed. After five steps, the error in the data reaches a plateau which indicates that the channel has been found. Then, we allow the algorithm to search for all the nine components of s_1 at once and the error starts decreasing again until it reaches the final plateau that indicates the end of the inversion process.

The next example considers a high-contrast medium with a single conducting, rectangular inclusion (see figure 10). In this example there is no channel of flow concentration so the asymptotic resistor network approximation does not apply. However, the medium can still be imaged remarkably well with our algorithm. The adjustable height of the maxima of the high-contrast module (4.6) is a key point for success. During the inversion process, one of the peaks of $f_j(\cdot)$ is suppressed while the remaining peak finds the correct location of the conducting inclusion. The image obtained is shown in figure 11. The magnitude of the conductivity of the

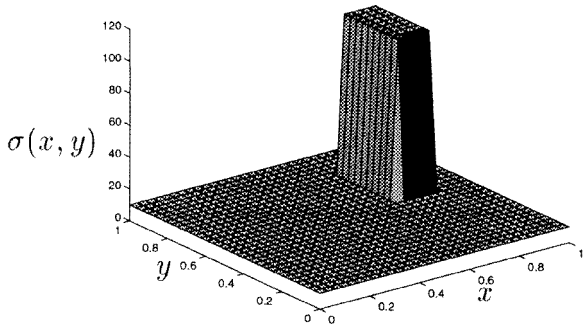

Figure 10. High-contrast model conductivity with one conducting square inclusion.

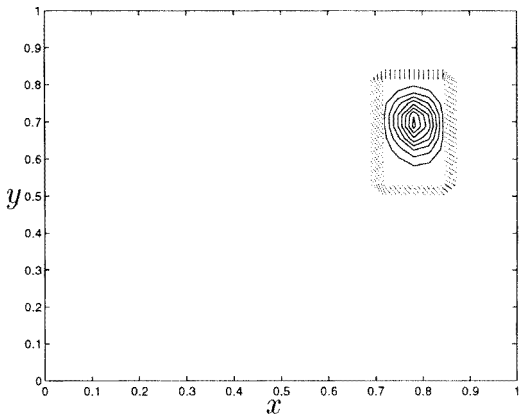

Figure 11. Contour plot of model conductivity (dotted curve) and reconstructed conductivity with high-contrast model (4.6) (full curve).

inclusion is, once again, not well approximated for the same reasons we explained before: first, our search is limited to functions $f_j(\cdot)$ given by (4.6). Second, the conductivity of maxima of σ is much harder to estimate than the conductivity of a channel. This is due to the negligible potential difference across a peak of the conductivity. This effect is highly visible in the experiments of section 5.1, where the maxima of σ are approximated by Gaussians. When imaging media with isolated inclusions, such as the example shown in figure 10, the high-contrast library performs essentially the same as a library of Gaussian functions. However, when we have inclusions that are close together so channels of strong flow develop, the high-contrast library is more successful. This follows because the high-contrast library was designed to image the channels that are the key part in inversion, as we show in section 3.

5.2. Intermediate contrast imaging

The asymptotic resistor network approximation described in section 2 is known to be accurate within a few per cent as long as the contrast in $\sigma(x)$ is of order 100 or higher (see [10]). Thus, it is expected that the inversion algorithm discussed in this paper performs well for such high contrasts. In this section we also test the algorithm for intermediate contrasts, that is contrasts of order one, which are too low for a very good approximation by the asymptotic theory but too high for the Born approximation to be justified.

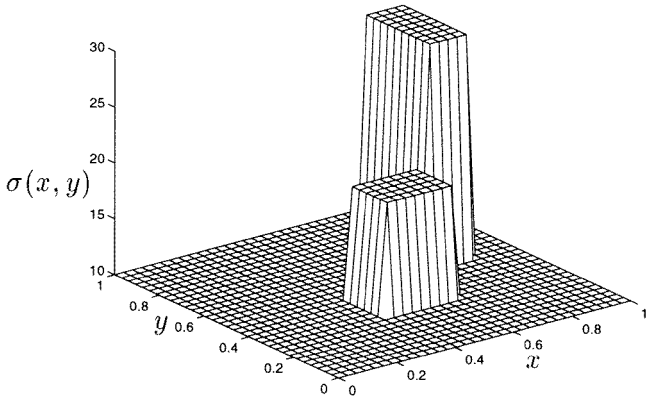

Figure 12. Intermediate contrast conductivity function.

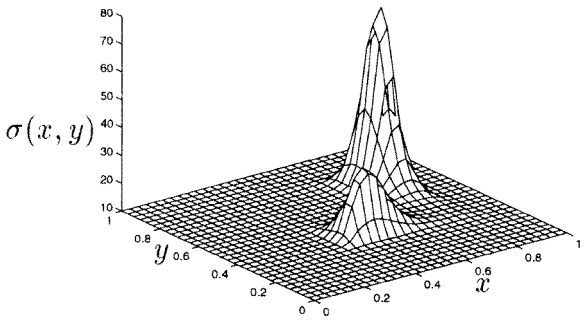

Figure 13. Conductivity reconstructed with cubic model.

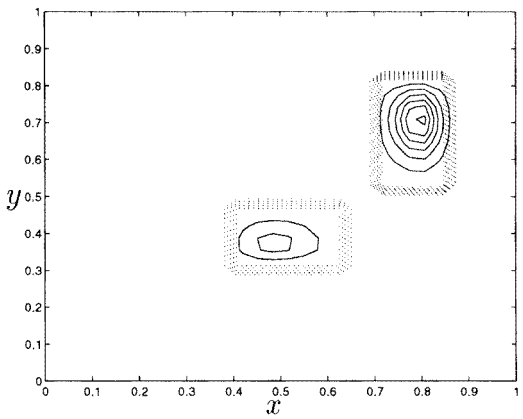

Figure 14. Contour plot of model conductivity (dotted curve) and reconstructed conductivity with high-contrast cubic model (4.6) (full curve).

We consider the numerical experiment of imaging the medium shown in figure 12, where in a uniform background conductivity $\sigma_b = 10$ we embed two square inclusions of conductivity $\sigma_1 = 20$ and $\sigma_2 = 30$. The image given by the high-contrast library described in section 3.2 is shown in figures 13 and 14. The algorithm proves its ability to localize correctly the inclusions

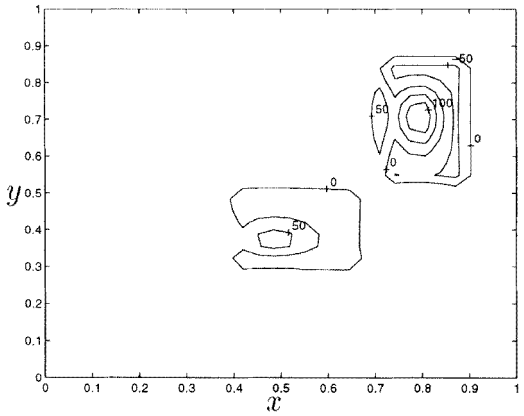

Figure 15. Error in the conductivity (%) for imaging with the cubic model.

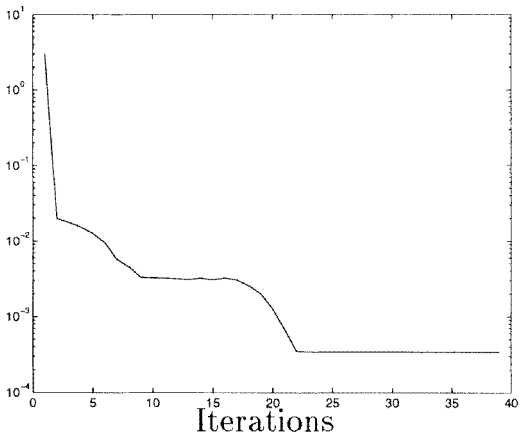

Figure 16. Error in the electric potential during the imaging process with the cubic model.

and to indicate which inclusion is the more conducting one. However, the magnitude of the conductivity of the inclusions is, once again, not very accurate and the actual ratio $\sigma_2/\sigma_1 = 1.5$ is not recovered in the image, but instead it is overestimated at 1.9367. In the high-contrast experiment presented in section 4.1, the inversion algorithm gave a very good estimate of the relative height of the two peaks of the conductivity. When the contrast is lowered and the asymptotic theory is not so accurate, the performance of the imaging algorithm is shown to deteriorate, as expected. However, the deterioration is not complete; the inclusions are still located in an accurate and efficient way. The relative error in the conductivity is shown in figure 15 and, as explained above, it is large only near the maxima of the conductivity. The evolution of the error in the electric potential at the boundary is shown in figure 16. The first dramatic drop in the energy is due to the estimate of the background conductivity σ_b. Then, we insert in the search a high-contrast module of form (4.6) and we search for the location of the inclusions (channel). In seven steps, the error reaches a plateau which indicates that the inclusions are found. Then, we search for all nine components of s (see (4.8)) and the uniform background σ_b, which causes the error to decrease again until we reach the final plateau in 22 steps.

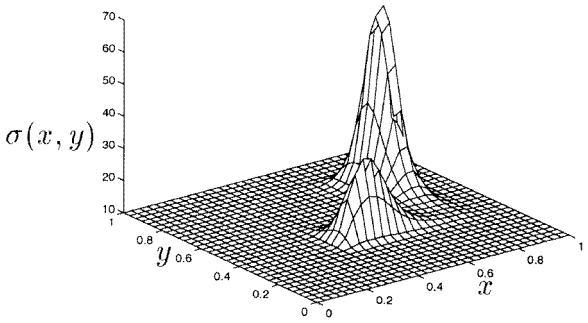

Figure 17. Conductivity reconstructed with cubic model from noisy data.

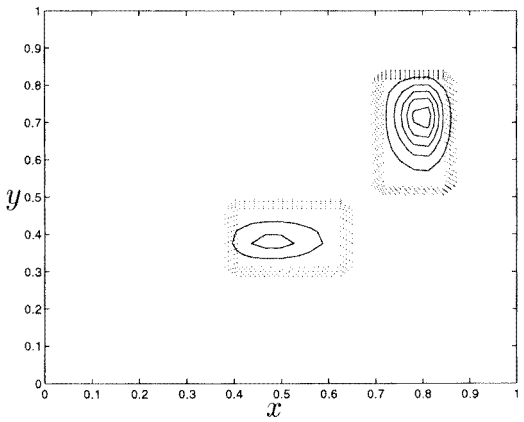

Figure 18. Contour plot of the model conductivity (dotted curve) and reconstructed conductivity with high-contrast cubic model (4.6) (full curve) from noisy data.

Next, we repeat the above experiment with noisy data, where we have 1% multiplicative noise (which is known to be typical of real data) in the measured electric potential at the boundary. The image obtained is shown in figures 17 and 18 and it is essentially equivalent to the image obtained with the noiseless data. Thus, the high-contrast library proves to be not only efficient in giving a good qualitative picture, but also robust and not very sensitive to noisy measurements typical of those found in practice. Other experiments, with the level of noise increased up to 5%, show results similar to those in figure 18. The localization of the inclusions remains essentially unchanged by the noise, only the magnitude of the conductivity near the maxima of $\sigma(\boldsymbol{x})$ seems to be affected.

6. Matching pursuit with other libraries

In this section we describe other libraries that may be used in a matching pursuit approach of imaging high- and intermediate-contrast conducting media. We discuss two such choices: Gaussians and wavelet libraries. We present numerical experiments and compare results with those obtained using the high-contrast library described in section 4.

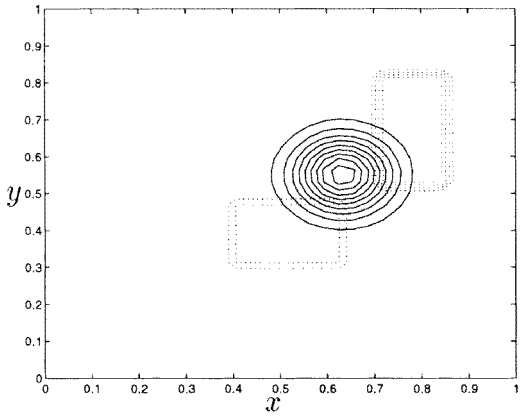

Figure 19. Contour plot of model conductivity (dotted curve) and reconstructed conductivity with one Gaussian search.

6.1. Library of Gaussian functions

One choice of high-contrast modules in (4.1), that is perhaps one of the first things one would try, is the approximation of the peaks of σ by Gaussians. Thus, we consider the functions

$$\begin{aligned} f_j(\boldsymbol{s}_j, x, y) &= \sigma_j \exp[-k_j\xi^2 - p_j\eta^2] \\ \xi &= (x - x_j)\cos\theta_j + (y - y_j)\sin\theta_j \\ \eta &= -(x - x_j)\sin\theta_j + (y - y_j)\cos\theta_j \end{aligned} \tag{6.1}$$

where the set of parameters is

$$\boldsymbol{s_j} = (\sigma_j, k_j, p_j, x_j, y_j, \theta_j). \tag{6.2}$$

Here σ_j gives the height of the peak, k_j and p_j are curvatures that also control the support of each peak, (x_j, y_j) is the location of the maximum and θ_j allows for arbitrary rotation in the plane. This model is attractive because it depends only on six parameters and it is more flexible than the previous ones by allowing, for example, an arbitrary distance between the peaks. However, numerical experiments show that in fact this model is not at all useful and leads to many difficulties. In order to identify a channel, we must search with at least two Gaussians at a time. If we just use one Gaussian, the algorithm will try to fit it over the channel and not on one of the maxima of σ. This behaviour is not surprising for two reasons: first, the asymptotic theory (see [10]) tells us that the saddle points and not the maxima of σ are the controlling features for the flow in Ω. Thus, the algorithm tries to minimize the error at the boundary by approximating somehow the effect of the channel through the peak of the Gaussian model. Second, this is a very well known behaviour of the method of matching pursuit [32] which is in fact the technique we are using in our attempt at recovering, one by one, the high-contrast features of σ. Even when we do the channel search using two Gaussians at a time, the numerical results are not satisfactory. We are in general able to locate the inclusions and the channels between fairly well but the magnitude of the peaks can grow without bound. This is a clear effect of the instability of the model that was completely eliminated before because the height of the peaks was implicitly connected with the conductivity in the channel (the essential feature in imaging high contrast σ).

We illustrate the results of two attempts to image the high-contrast conductivity shown in figure 6. In the first attempt, we search for the high-contrast features of σ with one Gaussian high-contrast model at a time. The contour plot of the final result is shown in figure 19 and, as

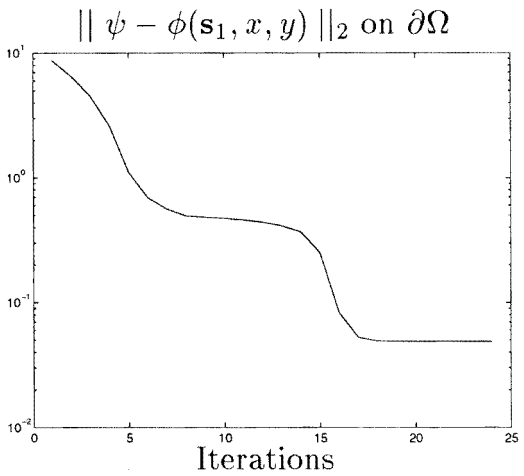

Figure 20. Evolution of the error in the potential at the boundary.

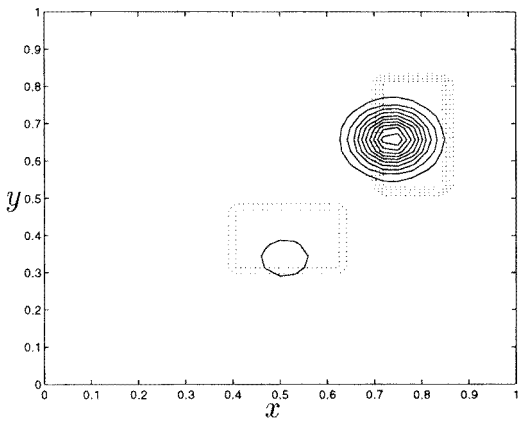

Figure 21. Contour plot of model conductivity (dotted curve) and reconstructed conductivity with two Gaussians search at a time.

we explained above, the high-contrast module is fitted to the channel and not to an actual peak of σ. The error of the potential at the boundary (see figure 20) is only slightly larger than the error given by the search with the cubic model (see figure 9). This is in fact quite misleading because with almost the same error at the boundary of the domain, we have in fact two very different results for the imaged conductivity. The result obtained with the cubic model is obviously more informative and close to the real σ. The result obtained with the Gaussian model leads us to the false conclusion that there is a peak in the region where we actually have a channel. When we try to improve the result shown in figure 19 by inserting another Gaussian module while the first one remains frozen into place, we observe that the second Gaussian merges with the first one and so the final result is still the one shown in figure 19, without any improvement.

Next, we search for the high-contrast features of σ with two Gaussian modules at a time. The contour plot of the reconstructed image is shown in figure 21 and we see that the location and support of the peaks of σ are well approximated. However, when we look at the reconstructed image (figure 22) and the actual σ we see that the error is very large. This follows

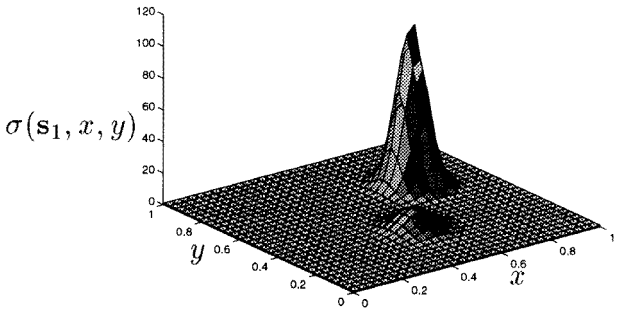

Figure 22. Reconstructed conductivity with two Gaussians at a time.

because the height of the peaks of the reconstructed image is a very poor approximation of the conductivity of the inclusions. Our result determines the more conducting inclusion quite well but the other inclusion is assigned a conductivity almost equal to the background. Other numerical experiments revealed cases where one peak of the reconstructed image was amplified by a factor as high as 10^4 whereas the other peak was greatly underestimated. The result obtained with the cubic model (see figure 7) is not very accurate either, but it is of the same order of magnitude as the model and the more conducting inclusion is correctly indicated to have σ twice the conductivity of the other inclusion.

6.2. Matching pursuit with an orthogonal wavelet dictionary

In the previous sections we treated the unknown conductivity function as a superposition of high-contrast modules. This decomposition was suggested by the asymptotic resistor network approximation (see section 3 and [10]) of flow in high-contrast media. Each module in decomposition (4.1) has a physical meaning because it represents a resistor in the asymptotic network. Decomposition (4.1) of the unknown σ is an idea that can be extended to any inversion process, independent of the contrast. This idea can be found under the name of *atomic decomposition* in the wavelet literature [33], where modules f_j bear the name *atoms*. In general, the number of modules needed for an accurate representation of σ is large, but in the high-contrast case only a few modules dominate, and they are associated with the channels of strong flow that develop in the medium. When the contrast is lowered and there is no flow channelling, the modules lose their physical meaning but nevertheless, the idea of atomic decomposition still applies. Thus, we view the unknown $\sigma(x, y)$ as

$$\sigma(x, y) = C_0 + \sum_{\lambda_n \in D} C_{\lambda_n} f_{\lambda_n}(\boldsymbol{s}_{\lambda_n}, x, y) \tag{6.3}$$

where D is a countable set and $\boldsymbol{s}_{\lambda_n}$ is a set of parameters that describes each module $f_{\lambda_n}(\cdot)$.

The family $F = \{f_{\lambda_n}(\cdot), \lambda_n \in D\}$ is in general redundant, but it can also be a basis of $L_2(\mathbb{R})$. We are interested in an efficient atomic decomposition of σ so the family F must be carefully chosen. The selection is highly dependent on what *a priori* information, if any, we have about σ. If, for example, we expect the medium to contain inclusions of various conductivity (not necessarily high contrast), the function σ will have various localized peaks in Ω. The spatial localization of the main features of σ leads us to the natural choice of F as a wavelet dictionary. In two dimensions, the wavelet dictionary consists of functions that are dilated, rotated, and translated in the domain [33].

Once we establish the family F, we attempt to reconstruct the conductivity σ iteratively, by adding one by one the modules belonging to F that give the smallest error of the potential

at the boundary. A sketch of the algorithm is given below.

Algorithm 6.1.
Step 1. *Choose the dictionary F*

$$D_0 = F,\ i = 0.$$

Step 2. *Look for* $f_{\lambda_{i+1}}(\cdot) \in D_i$ *that gives the smallest error at the boundary, and estimate* $C_{\lambda_{i+1}}$

$$\sigma_{i+1}(x, y) = \sigma_i(x, y) + C_{\lambda_{i+1}} f_{\lambda_{i+1}}(x, y)$$
$$i = i + 1,\ D_i = D_{i-1} \backslash \{f_{\lambda_i}\}.$$

Step 3. *Correct coefficients* C_{λ_j}, $j = 0, \ldots, i$.
Repeat steps 2 and 3 to improve the image.

The algorithm is very close in spirit to the *matching pursuit* algorithm described in [32]. However, in [32] the function that is decomposed is known and the choice of each module f_{λ_i} is based upon maximizing the coefficients C_{λ_i}. Another important difference is that, after we find each f_{λ_i}, we readjust all the coefficients in the current decomposition. Step 3 in algorithm 6.1 has proved to be very important for two reasons. First, by adding each module, we include more information about σ which helps us get better and better estimates of previous C_{λ_i}. Second, by readjusting the constants after each step, we can easily decide when to stop the inversion process. This becomes quite clear in the following example.

We consider a model conductivity given by

$$\sigma(x, y) = 15 + 100\psi_{0,1,1,0}(x, y) + 100\psi_{0,1,1,3}(x, y) \tag{6.4}$$

where $\psi_{m,i,j,k}$ are Daubechies' orthogonal wavelets defined at scale 2^m and centred at point $(i/2^m, j/2^m)$ [16]. Index $k \in \{0, 1, 2, 3\}$ indicates which function $\psi(\cdot)$ to choose. Since we are in two dimensions, the choices are: $\psi =$ product of two father wavelets for $k = 0$, product of a mother and a father wavelet for $k = 1, 2$ and product of two mother wavelets for $k = 3$, respectively. We consider 15 sets of data values of the potential at the boundary $\partial\Omega$. Each set corresponds to a different current excitation pattern. The potential is measured at 32 uniformly distributed points along each side of the square $\partial\Omega$. The family of functions F considered in our search consists of Daubechies' two-dimensional orthogonal wavelets up to resolution $m = 3$. Thus, the dictionary consists of 340 modules. The evolution of the error at the boundary during the reconstruction process is shown in figure 23. The initial error is 1.93 and the initial conductivity is $\sigma_0(x, y) = 1$. We look for the best constant σ to fit the data and find $\sigma_1 = 13.7$ which makes the data error 9.32×10^{-2}. The next step identifies the module $\psi_{0,1,1,0}(x, y)$ and estimates the coefficient $C_1 \sim 75.26$. The data error at this point is 8.75×10^{-2}. We readjust the constants and find $C_0 \sim 14.3$ and $C_1 \sim 87.3$. The data error is 8.51×10^{-2}. Next, we find the second wavelet $\psi_{0,1,1,3}(x, y)$, with coefficient $C_2 \sim 65.34$. The data error is 7.41×10^{-2}. Even though at this point we identified all the modules in the decomposition of σ, the data error did not change much during the last three steps. This is of course due to the inaccurate constants C_j. Thus, we readjust the constants and find $C_0 = 15.0001$, $C_1 = 99.999\,91$ and $C_2 = 100.02$. After this final step we find that the error in the potential at the boundary drops dramatically to 7.34×10^{-9}, which is a clear indication that we should stop the reconstruction process, having achieved our data fitting objective.

The algorithm performs very well in the above example mainly because the model $\sigma(x, y)$ has an exact representation in terms of a few terms of the finite dictionary that was chosen *a priori*. For a general $\sigma(x, y)$ this will not be so, and we will need a much larger number of modules to get an acceptable image. The question is how to choose the dictionary that will allow us an efficient representation of σ in terms of a small number of modules. The orthogonal

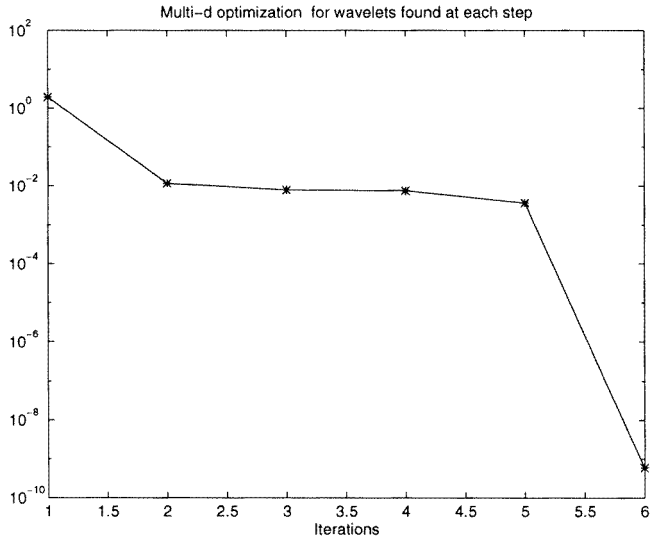

Figure 23. Evolution of error in the electrical potential at the boundary.

basis of orthogonal Daubechies' wavelets, while sufficient for representing σ, is not efficient because it is too rigid; it only allows scales in powers of two and particular locations. For example, if our σ has a peak that coincides with the peak of a wavelet in the dictionary, then it is easy to recover. However, if the peak is slightly moved, we need many modules to represent it.

6.3. Adaptive Mexican hat dictionary

The limitations of a wavelet basis in the imaging process lead us naturally to the idea of an adaptive dictionary of wavelet functions where we can have arbitrary translations, dilations and rotations of the modules. We choose each module as a product of two Mexican hat wavelets:

$$\begin{aligned} f_j(\boldsymbol{s}_j, x, y) &= \psi(\xi, \alpha_j)\psi(\eta, \beta_j) \\ \xi &= (x - x_j)\cos\theta_j + (y - y_j)\sin\theta_j \\ \eta &= -(x - x_j)\sin\theta_j + (y - y_j)\cos\theta_j \end{aligned} \tag{6.5}$$

where

$$\psi(\xi, \alpha) = 2\sqrt{\frac{\alpha}{3}}(1 - \alpha^2\xi^2)\,\mathrm{e}^{-\alpha^2\xi^2}. \tag{6.6}$$

The vector of parameters $\boldsymbol{s}_j = (x_j, y_j, \alpha_j, \beta_j, \theta_j)$ gives the location (x_j, y_j), dilation α_j, β_j and orientation θ_j of each module f_j. Instead of limiting these parameters to a discrete number of values, we allow them to vary arbitrarily during the inversion process. The sketch of the inversion algorithm is the following.

Algorithm 6.2.

$i = 0$.

Step 1. *Find optimal $\boldsymbol{s}_i$ by minimizing the error at the boundary.*

$$\begin{aligned} &\sigma_{i+1}(x, y) = \sigma_i(x, y) + C_i f_i(x, y) \\ &i = i + 1. \end{aligned}$$

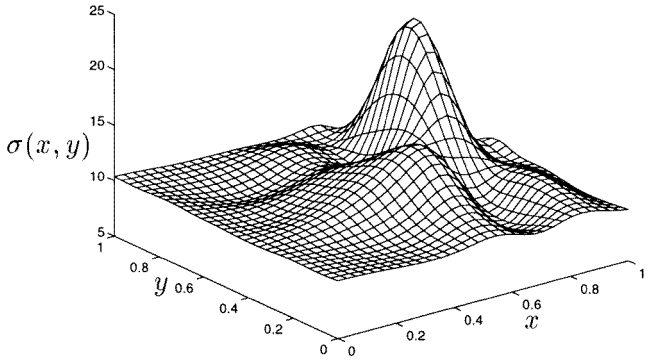

Figure 24. Conductivity reconstructed with Mexican hat wavelets.

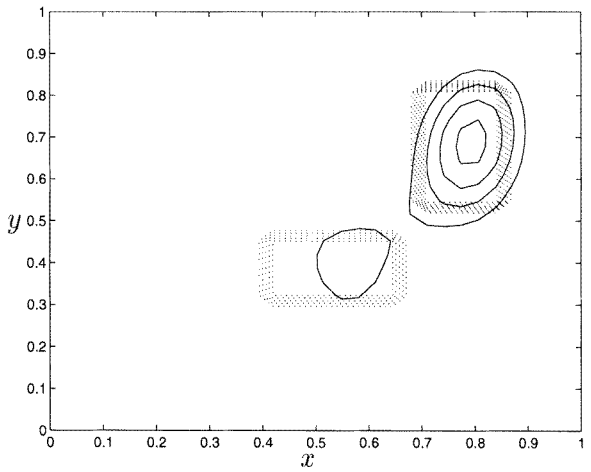

Figure 25. Contour plot of the model conductivity (dotted curve) and the image obtained with Mexican hat wavelets (full curve).

Step 2. *Correct coefficients* C_j, $j = 0, \ldots i$.

Repeat steps 1 and 2 to improve the image.

We return to the numerical experiment of imaging the intermediate-contrast medium shown in figure 12, but this time we use Algorithm 6.2, with a library of Mexican hat wavelets. The image obtained is shown in figures 24 and 25. Clearly, the image captures well the location of the inclusions and it gives a good estimate of the ratio of the conductivities: $\sigma_2/\sigma_1 = 1.4672$ as opposed to the actual value of 1.5. Furthermore, the relative error in the image conductivity is shown in figure 26 to be no more than 40%, which is a significant improvement over the result obtained with the high-contrast library (see figure 15). The image is given by a combination of ten wavelets, where the insertion of each wavelet in the search is indicated by the increase in the error at the boundary, as shown in figure 28. After each wavelet enters the search, it takes about 20 steps to find the optimal set of parameters s_i, $i = 1, \ldots, 10$ that describes it. In figure 27 we show a simplified picture of the error in the potential at the boundary, where each iteration means finding a set s_i that describes the ith wavelet in the search. However, finding each wavelet implies doing about 20 iterations, as shown in figure 28. Thus, the wavelet dictionary is more expensive in computation time than the high-contrast library, but the image is better.

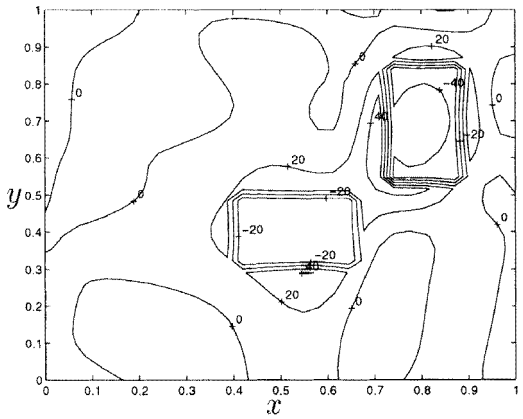

Figure 26. Error in the image conductivity (%) obtained with Mexican hat wavelets.

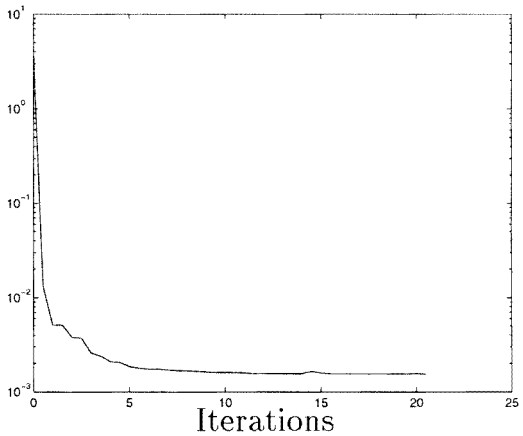

Figure 27. Error in the electric potential at the boundary for imaging with Mexican hat wavelets.

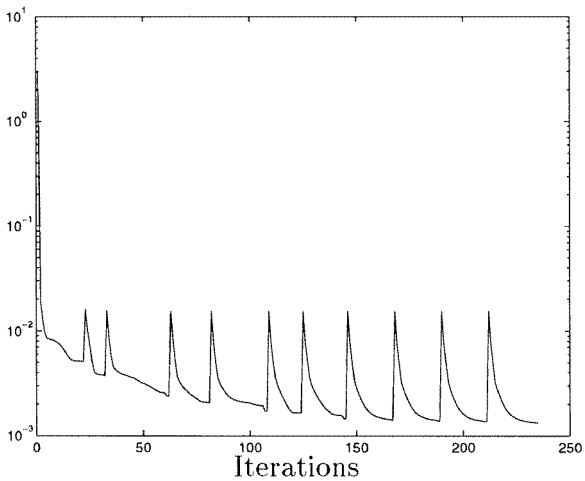

Figure 28. Detailed picture of the error in the electric potential at the boundary for imaging with Mexican hat wavelets.

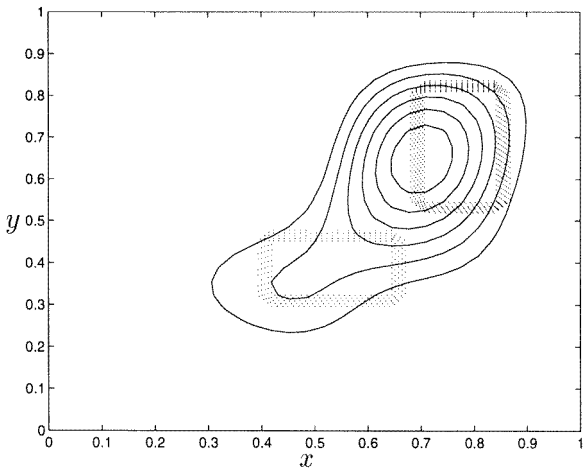

Figure 29. Contour plot of the model conductivity (dotted curve) and the image obtained with Mexican hat wavelets (full curve) from noisy data.

Next, we repeat the experiment with the 1% multiplicative noise added to the potential at the boundary. The image given by the wavelet library is shown in figure 29 and it is much worse than the noiseless one because the location of the inclusions is not well estimated. Hence, the wavelet library appears very sensitive to noise, whereas the high-contrast library is more robust and efficient at the same time. Notice that, to obtain the image of figure 29, we use 20 modules f_j given by (23) or, equivalently, 100 parameters. This large number of parameters allows algorithm 6.2 enough freedom to fit the noise at the expense of the quality of the image. Thus, an algorithm that trades off the complexity of the model and data fit [1, 36] must be used for the wavelet library. The high contrast library requires only nine parameters and so, it is not surprising that it is more robust with respect to noise.

Finally, the performance of the wavelet library deteriorates as the contrast in σ increases. Numerical experiments show that, for high contrasts, the wavelet library experiences difficulties similar to those of the Gaussians. Thus, in the first steps of the inversion, the algorithm tries to account for the channels developed between nearby inclusions by fitting spurious peaks over them. Then, in later steps, there is a lot of computation time needed for correcting the initial mistakes, which makes the method very inefficient.

7. Summary

We have presented a matching pursuit approach for imaging high-contrast and intermediate-contrast conducting media. We have shown that matching pursuit can be used successfully and effectively for inversion if the library of functions is constructed in accordance with the asymptotic theory for current flow in high-contrast media. The analysis shows that flow in high-contrast media can be approximated by current through a resistor network. The network accounts for flow channelling effects that develop at saddle points of the conductivity function $\sigma(\boldsymbol{x})$ or in channels or gaps between nearby high-contrast features. We have shown that, as the contrast goes to infinity, the Neumann to Dirichlet map associated with the imaging problem is equivalent to the Neumann to Dirichlet map of the asymptotic resistor network. Thus, as shown in [14, 15], the high-contrast features of $\sigma(\boldsymbol{x})$ that are contained in the resistor network approximation can be uniquely recovered, in general. Based on the asymptotic theory,

we introduce a parametrization of the high-contrast features of $\sigma(\boldsymbol{x})$ in terms of a library of high-contrast functions. We have shown through numerical experiments that this library gives efficient construction of good, qualitative images of intermediate- and high-contrast media. Moreover, numerical experiments with noisy data show that the high-contrast library is robust and not very sensitive to noise. We have also experimented with other libraries of functions such as wavelets and Gaussians. Our numerical experiments show that the high-contrast library is far superior to the other choices in both the quality of the images and the efficiency with which the main features of the images can be reconstructed.

Acknowledgments

The work of L Borcea was supported by the National Science Foundation under grant number DMS-9627407.

The work of J G Berryman was performed under the auspices of the US Department of Energy by the Lawrence Livermore National Laboratory under contract no W-7405-ENG-48 and supported in part by the Environmental Management Science Program of the DOE, with oversight from the Engineering Research Division in the Office of Basic Energy Sciences, Office of Energy Research, and from the Office of Science and Technology, Office of Environmental Management.

Work of G C Papanicolaou was partially supported by a grant from AFOSR, F49620-98-1-0211 and by the NsF, DMS 96228554.

Appendix A. Choosing trial fields for general boundary excitations

In this appendix we explain how to choose the trial fields $H(x)$ in the variational principle (3.28), for general current excitations I at the boundary. Inside the domain Ω, $H(\boldsymbol{x})$ is chosen as (3.30). Outside a thin layer at $\partial\Omega$ and in the basins of attraction of the minima of σ, the field H is constant. The constant value of H in the basin of attraction of a minimum $\boldsymbol{x}'_j$ near the boundary, is chosen as

$$H(\boldsymbol{x}) = h(s_{j'}) \tag{A.1}$$

where $j' \in \mathcal{N}'_{\mathrm{B}}$ is the boundary node in the dual network that is associated with the minimum $\boldsymbol{x}'_j$ of σ. More precisely, $s_{j'}$ is the intersection between $\partial\Omega$ and the ridge of minimal conductivity through $\boldsymbol{x}'_j$. To match the boundary conditions

$$H(\boldsymbol{x}) = h(s) = -\int^{s} I(t)\,\mathrm{d}t \tag{A.2}$$

we introduce thin layers at the boundary where we extend the field H from the boundary values (A.2) to the desired form (3.30) inside Ω.

For simplicity of explanation, we choose a piece of the boundary that is between two adjacent dual nodes a' and b', as shown in figure A.1. These nodes correspond to the minima $\boldsymbol{x}_{a'}$ and $\boldsymbol{x}_{b'}$ of the conductivity. The broken line is a ridge of minimal conductivity and it delimits the basin of attraction of the maximum $\boldsymbol{x}_a$ of σ that is associated with the boundary node a. To extend the boundary function $h(s)$ inside, we choose a non-uniform layer as shown in figure A.1. The layer has constant thickness δ on the part of the boundary where the conductivity increases in the normal, inward direction t. Near the dual nodes a' and b', σ increases in the direction of the normal, so we choose a variable thickness of the layer. In figure A.1, the $a'M$ margin of the layer is chosen such that σ increases from a' towards M. Likewise, σ increases from b' towards N.

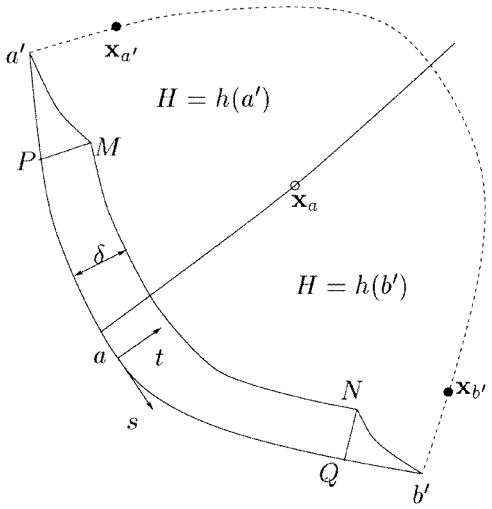

Figure A.1. Thin layer at the boundary where the field H changes from the given $h(s)$ to the desired form (3.30).

We wish to calculate the integral

$$\int_{\text{layer}} \frac{1}{\sigma(\boldsymbol{x})}|\nabla^{\perp}H|^2\,\mathrm{d}\boldsymbol{x} = \int_{PMNQ} \frac{1}{\sigma(\boldsymbol{x})}|\nabla^{\perp}H|^2\,\mathrm{d}\boldsymbol{x} + \int_{a'PM} \frac{1}{\sigma(\boldsymbol{x})}|\nabla^{\perp}H|^2\,\mathrm{d}\boldsymbol{x} + \int_{b'QN} \frac{1}{\sigma(\boldsymbol{x})}|\nabla^{\perp}H|^2\,\mathrm{d}\boldsymbol{x} \tag{A.3}$$

and show that it is small. In the uniform piece of the boundary layer $MNPQ$, we choose the trial field H as an harmonic function that satisfies

$$H(s,t) = \begin{cases} \dfrac{h(b')-h(a')}{2}\operatorname{erf}\left(\dfrac{s-s_a}{\sqrt{2k\epsilon}}\right) + \dfrac{h(a')+h(b')}{2} & \text{if } t = \delta \\ h(s) & \text{if } t = 0 \end{cases} \tag{A.4}$$

where k is the curvature of σ, at the point (s_a, δ), in the direction s. Then, the current in region $PMNQ$ is of the order

$$|\boldsymbol{j}|^2 = |\nabla^{\perp}H|^2 \leqslant \frac{K_1}{\delta^2} + \frac{K_2}{\epsilon}\,\mathrm{e}^{-k(s-s_a)^2/\epsilon} \tag{A.5}$$

where K_1 and K_2 are two positive and bounded constants; the first term accounts for the change of H in direction t and the last term is due to the large current that we impose near $s = s_a$. Furthermore, the conductivity σ increases in direction t, so we have

$$\sigma(s,t) \approx \sigma(s,0)\,\mathrm{e}^{p(s)t/\epsilon} \qquad \text{where } p(s) > 0. \tag{A.6}$$

Thus,

$$\int_{PMNQ} \frac{1}{\sigma(\boldsymbol{x})}|\nabla^{\perp}H|^2\,\mathrm{d}\boldsymbol{x} \leqslant \int_{s_P}^{s_Q} \mathrm{d}s\,\frac{1}{\sigma(s,0)}\int_0^{\delta}\mathrm{d}t\,\mathrm{e}^{-p(s)t/\epsilon}\left[\frac{K_1}{\delta^2} + \frac{K_2}{\epsilon}\,\mathrm{e}^{-k(s-s_a)^2/\epsilon}\right]$$
$$\lesssim D_1\frac{\epsilon}{\delta^2} + D_2\sqrt{\epsilon} \tag{A.7}$$

where D_1 and D_2 are two bounded, positive constants.

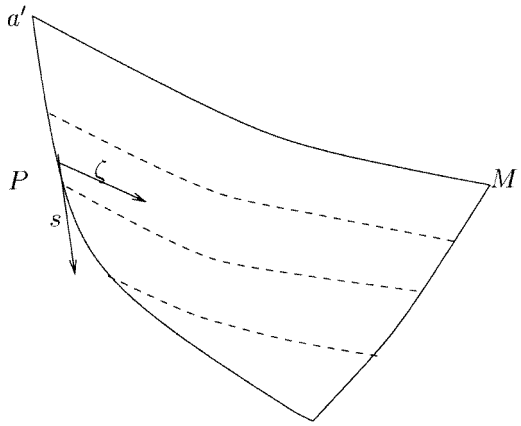

Figure A.2. The region $a'PM$ is divided into thin strips.

In the region $a'PM$, the field H is chosen as an harmonic function that is equal to $h(s)$ along $a'P$ and $h(a')$ along $a'M$. Thus, the current in $a'PM$ is of the order

$$|\boldsymbol{j}|^2 = |\nabla^\perp H|^2 \leqslant K_1/\delta^2 \tag{A.8}$$

where K_1 is a bounded, positive constant. To calculate $\int_{a'PM}[1/\sigma(\boldsymbol{x})]|\nabla^\perp H|^2\,\mathrm{d}\boldsymbol{x}$, we divide the region $a'PM$ into thin strips, as shown in figure A.2. In each strip, we have

$$\sigma(s,\zeta) \approx \sigma(s,0)\,\mathrm{e}^{p(s)\zeta/\epsilon} \tag{A.9}$$

where ζ is in the direction of increase of σ and $p(s) > 0$. Then,

$$\int_{a'PM} \frac{1}{\sigma(\boldsymbol{x})}|\nabla^\perp H|^2\,\mathrm{d}\boldsymbol{x} \lesssim D_1\frac{\epsilon}{\delta^2} \tag{A.10}$$

where D_1 is a bounded, positive constant. Similarly, we obtain that

$$\int_{b'QN} \frac{1}{\sigma(\boldsymbol{x})}|\nabla^\perp H|^2\,\mathrm{d}\boldsymbol{x} \lesssim D_1\frac{\epsilon}{\delta^2}. \tag{A.11}$$

Thus, by letting the width of the layer $\delta \to 0$ such that $\delta^2/\epsilon \to \infty$ as $\epsilon \to 0$, we obtain that, for our trial current, the power dissipated near the boundary is negligible in comparison with the power dissipated at the saddle points of σ. Note that all the calculations in this appendix are based on the assumption that there is no saddle point of σ on the boundary. If there is a saddle point at the boundary, the vicinity of that saddle gives a significant contribution to the integral $\int_\Omega[1/\sigma(\boldsymbol{x})]|\nabla^\perp H|^2\,\mathrm{d}\boldsymbol{x}$ and it must be included in the upper bound of lemma 2.

Appendix B. Regularization method

In this appendix we present the regularization method used to stabilize the least-squares problem of finding the set of parameters $\boldsymbol{s} \in \mathbb{R}^p$ that is consistent with the boundary data in the inversion process and that describes the conductivity $\tilde{\sigma}(\boldsymbol{x};\boldsymbol{s})$ given by (4.1). The optimal set of parameters $\boldsymbol{s}$ minimizes the error in the potential measured at the boundary. We use the notation

$$\begin{aligned}
&\boldsymbol{\Psi} = (\psi_k^{(i)})_{k=1,\ldots,N;i=1,\ldots,M}\\
&\boldsymbol{\Phi}(\boldsymbol{s}) = (\phi(\boldsymbol{s})_k^{(i)})_{k=1,\ldots,N;i=1,\ldots,M}\\
&\boldsymbol{\Psi},\ \boldsymbol{\Phi} \in \mathbb{R}^{NM}
\end{aligned} \tag{B.1}$$

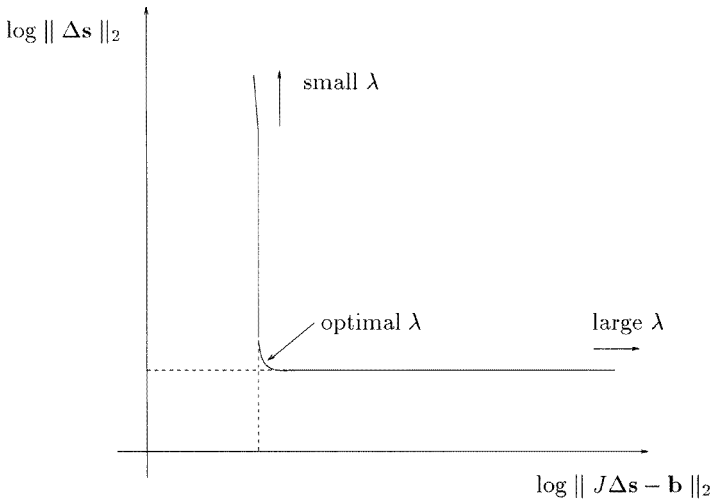

Figure B.1. Schematic L-curve.

where $\psi_k^{(i)}$ represents the measured potential at the point k along the boundary, for the ith pattern of current excitation, and $\phi(s)_k^{(i)}$ is the potential obtained with the model conductivity $\sigma(\boldsymbol{s}, \boldsymbol{x})$. Hence, the optimal set of parameters is the solution of the nonlinear least-squares problem

$$\min_{\boldsymbol{s}} \|\boldsymbol{\Psi} - \boldsymbol{\Phi}(\boldsymbol{s})\|_2. \tag{B.2}$$

We solve (B.2) with a Gauss–Newton iterative method, so at step n we have the linear least-squares problem

$$\begin{aligned} &\min_{\Delta \boldsymbol{s}} \|\boldsymbol{\Psi} - \boldsymbol{\Phi}(\boldsymbol{s}^n) - J(\boldsymbol{s}^n)\Delta \boldsymbol{s}\|_2 \\ &\boldsymbol{s}^{n+1} = \boldsymbol{s}^n + \Delta \boldsymbol{s} \end{aligned} \tag{B.3}$$

where J is the Jacobian matrix $\partial \boldsymbol{\Phi}(\boldsymbol{s}^n)/\partial \boldsymbol{s} \in \mathbb{R}^{NM \times p}$. Due to the wide range of influence of the components of $\boldsymbol{s}$ on the potential Φ, the Jacobian matrix is usually ill-conditioned. Hence, we use Tikhonov regularization to compute a stable solution of the ill-conditioned problem (B.3).

Now we address the problem of computing

$$\Delta \boldsymbol{s}_\lambda = \arg\min[\|J\Delta \boldsymbol{s} - \boldsymbol{b}\|_2^2 + \lambda^2 \|\Delta \boldsymbol{s}^2\|_2^2] \tag{B.4}$$

where

$$\boldsymbol{b} = \boldsymbol{\Psi} - \boldsymbol{\Phi}(\boldsymbol{s}^n).$$

The regularization parameter λ is chosen by means of the L-curve (see figure B.1), as described in [19–21]. This curve is a plot of the norm of the solution $\|\Delta \boldsymbol{s}\|_2$ versus the norm of the residual $\|J\Delta \boldsymbol{s} - \boldsymbol{b}\|_2$, where λ is a positive parameter. Let us consider the singular value decomposition of the Jacobian matrix

$$J = U\Gamma V^{\mathrm{T}}$$

where $U \in \mathbb{R}^{NM \times NM}$, $V \in \mathbb{R}^{p \times p}$ are orthogonal matrices and

$$\Gamma = \begin{pmatrix} \gamma_1 & & \\ & \ddots & \\ & & \gamma_p \\ & 0 & \end{pmatrix} \in \mathbb{R}^{NM \times p}$$

is the matrix of (non zero) singular values. The solution of (B.4) is

$$\Delta \boldsymbol{s}_\lambda = \sum_{i=1}^{p} f_i \frac{\boldsymbol{u}_i^{\mathrm{T}} \cdot \boldsymbol{b}}{\gamma_i} \boldsymbol{v}_i \tag{B.5}$$

where $\boldsymbol{u}_i$ and $\boldsymbol{v}_i$ are the columns of the orthogonal matrices U and V, respectively and f_i are the Tikhonov filters

$$f_i \begin{cases} \dfrac{\gamma_i^2}{\gamma_i^2 + \lambda^2} & \text{if } \gamma_i < \lambda \\ 1 & \text{otherwise.} \end{cases} \tag{B.6}$$

With the notation $\alpha_i = \boldsymbol{u}_i^{\mathrm{T}} \cdot \boldsymbol{b}$, we obtain

$$\eta(\lambda) = \|\Delta \boldsymbol{s}\|_2^2 = \sum_{i=1}^{p} \frac{\gamma_i^2 \alpha_i^2}{(\gamma_i^2 + \lambda^2)^2}$$

and

$$\rho(\lambda) = \|J \Delta \boldsymbol{s} - \boldsymbol{b}\|_2^2 = \sum_{i=1}^{p} \frac{\lambda^4 \alpha_i^2}{(\gamma_i^2 + \lambda^2)^2} + \|\boldsymbol{r}_\perp\|_2^2$$

where $\boldsymbol{r}_\perp$ is the part of $\boldsymbol{b}$ that is perpendicular to the columns of U, $\boldsymbol{u}_i$, $i = 1, \ldots, p$. Straightforward calculations show that

$$\begin{cases} \mathrm{d}\eta/\mathrm{d}\rho = -1/\lambda^2 \\ \dfrac{\mathrm{d}^2\eta}{\mathrm{d}\rho^2} = 1 \Big/ 2\lambda^6 \displaystyle\sum_{i=1}^{p} \frac{\lambda^4 \alpha_i^2}{(\gamma_i^2 + \lambda^2)^2} > 0. \end{cases} \tag{B.7}$$

Hence, the L-curve is convex and it becomes steeper as λ decreases towards the smallest singular value of the Jacobian matrix J. Furthermore, the error in $\Delta \boldsymbol{s}$ is

$$\Delta \boldsymbol{s}_\lambda - \Delta \boldsymbol{s} = \sum_{i=1}^{p} f_i \frac{\boldsymbol{u}_i^{\mathrm{T}} \cdot \boldsymbol{e}}{\gamma_i} \boldsymbol{v}_i + \sum_{i=1}^{p} (f_i - 1) \frac{\boldsymbol{u}_i^{\mathrm{T}} \cdot \boldsymbol{b}}{\gamma_i} \boldsymbol{v}_i \tag{B.8}$$

where $\boldsymbol{e}$ is the error in the vector $\boldsymbol{b}$. Thus, the left branch of the L-curve corresponds to less regularization or, equivalently, to $f_i \approx 1$, $i = 1, \ldots, p$ and the perturbation error dominates. Due to small singular values, for a small regularization parameter λ, $\|\Delta \boldsymbol{s}\|_2$ varies dramatically while the residual $\|J \Delta \boldsymbol{s} - \boldsymbol{b}\|_2$ remains almost the same. The right branch of the L-curve corresponds to a high degree of regularization, so most filters $f_i \ll 1$ and the regularization error dominates. Furthermore, due to the large regularization parameter λ, the update $\|\Delta \boldsymbol{s}\|^2$ is very small. Hence, the optimal regularization parameter λ balances the perturbation error and the regularization error in $\Delta \boldsymbol{s}_\lambda$. It is known (see [19]) that this optimal λ is not far from the regularization parameter that corresponds to the corner of the L-curve. The corner of the L-curve is defined as the point of maximum curvature or, equivalently

$$\lambda_{\text{optimal}} \approx \arg\max_{\lambda} K(\lambda) \tag{B.9}$$

where the curvature is given by

$$K(\lambda) = \frac{\rho'(\lambda)\eta''(\lambda) - \rho''(\lambda)\eta'(\lambda)}{[(\rho'(\lambda))^2 + (\eta'(\lambda))^2]^{3/2}}. \tag{B.10}$$

In our numerical computations we use the regularization method described above and the Matlab software written by Per Christian Hansen [20].

References

[1] Akaike H 1974 A new look at the statistical model identification *IEEE Trans. Automatic Control* **19** 716–23

[2] Batchelor G K and O'Brien R W 1977 Thermal or electrical conduction through a granular material *Proc. R. Soc.* A **355** 313–33

[3] Bank E R 1997 *PLTMG: A Software Package for Solving Elliptic Partial Differential Equations* (Philadelphia, PA: SIAM)

[4] Bender C M and Orszag S A 1978 *Advanced Mathematical Methods for Scientists and Engineers* (New York: McGraw-Hill)

[5] Berryman J G 1991 Convexity properties of inverse problems with variational constraints *J. Franklin Inst.* **328** 1–13

[6] Berryman J G and Kohn R V 1990 Variational constraints for electrical impedance tomography *Phys. Rev. Lett.* **65** 325–8

[7] Borcea L 1996 Direct and inverse problems for transport in high contrast media *PhD Thesis* Stanford University

[8] Borcea L 1999 Asymptotic analysis of quasistatic transport in high contrast conductive media *SIAM J. Appl. Math.* **59** 597–639

[9] Borcea L, Berryman J G and Papanicolaou G C 1996 High contrast impedance tomography *Inverse Problems* **12** 935–58

[10] Borcea L and Papanicolaou G C 1998 Network approximation for transport properties of high contrast materials *SIAM J. Appl. Math.* **58** 501–39

[11] Borcea L and Papanicolaou G C 1997 A hybrid numerical method for high contrast conductivity problems *J. Comput. Appl. Math.* **87** 61–78

[12] Cherkaeva E and Tripp A 1996 Inverse conductivity problem for noisy measurements *Inverse Problems* **12** 869–83

[13] Courant R and Hilbert D 1953 *Methods of Mathematical Physics* vol I (New York: Wiley) pp 240–2 (Dirichlet's principle) and pp 267–8 (Thomson's principle)

[14] Curtis E B and Morrow J A 1990 Determining the resistors in a network *SIAM J. Appl. Math.* **50** 931–41

[15] Curtis E B, Ingerman D and Morrow J A 1998 Circular planar graphs and resistor networks *Linear Algebra Appl.* **283** 115–50

[16] Daubechies I 1992 *Ten Lectures on Wavelets* (Philadelphia, PA: SIAM)

[17] Dobson D C and Santosa F 1994 Resolution and stability analysis of an inverse problem in electrical impedance tomography: dependence on the input current patterns *SIAM J. Appl. Math.* **54** 1542–60

[18] Grünbaum F A and Zubelli J P 1992 Diffuse tomography: computational aspects of the isotropic case *Inverse Problems* **8** 421–33

[19] Hansen P C 1992 Analysis of discrete ill-posed problems by means of the L-curve *SIAM Rev.* **34** 561–80

[20] Hansen P C 1993 Regularization Tools. A Matlab package for analysis and solution of discrete ill-posed problems *Report* UNIC-92-03. Available in PostScript form via Netlib (`netlib@research.att.com`) from the library NUMERALGO

[21] Hansen P C and O'Leary D P 1993 The use of the L-curve in the regularization of discrete ill-posed problems *SIAM J. Sci. Comput.* **14** 1487–503

[22] Isaacson D and Cheney D 1990 Inverse problems in partial differential equations *Current Problems in Impedance Imaging* ed D Colton, R Ewing and W Rundell (Philadelphia, PA: SIAM) pp 141–9

[23] Isakov V 1993 Uniqueness and stability in multi-dimensional inverse problems *Inverse Problems* **9** 579–621

[24] Jackson J D 1974 *Classical Electrodynamics* 2nd edn (New York: Wiley)

[25] Keller G V 1988 Rock and mineral properties *Electromagnetic Methods in Applied Geophysics vol 1, Theory* ed M N Nabighian (Tulsa, OK: Society of Exploration Geophysics) pp 13–52

[26] Keller J B 1963 Conductivity of a medium containing a dense array of perfectly conducting spheres or cylinders or nonconducting cylinders *J. Appl. Phys.* **34** 991–3

[27] Keller J B 1987 Effective conductivity of periodic composites composed of two very unequal conductors *J. Math. Phys.* **28** 2516–20

[28] Kohn R V and McKenney A 1990 Numerical implementation of a variational method for electrical impedance tomography *Inverse Problems* **6** 389–414

[29] Kohn R and Vogelius M 1985 Determining conductivity by boundary measurements *Commun. Pure Appl. Math.* **38** 643–67

[30] Kohn R and Vogelius M 1987 Relaxation of a variational method for impedance computed tomography *Commun. Pure Appl. Math.* **XL** 745–77

[31] Kozlov S M 1989 Geometric aspects of averaging *Russian Math. Surveys* **44** 91–144

[32] Mallat S and Zhang Z 1993 Matching pursuit in a time–frequency dictionary *IEEE Trans. Signal Processing* **41** 3397–415

[33] Meyer Y 1993 *Wavelets, Algorithms and Applications* (Philadelphia, PA: SIAM)
[34] Nachman A I 1995 Global uniqueness for a two-dimensional inverse boundary value problem *Ann. Math.* **142** 71–96
[35] Santosa F and Vogelius M 1990 A backprojection algorithm for electrical impedance imaging *SIAM J. Appl. Math.* **50** 216–43
[36] Schwartz G 1978 Estimating the dimension of a model *Ann. Statist.* **6** 461–4
[37] Somersalo E, Cheney M, Isaacson D and Isaacson E 1991 Layer stripping: a direct numerical method for impedance imaging *Inverse Problems* **7** 899–926
[38] Sylvester J and Uhlmann G 1990 The Dirichlet to Neumann map and applications *Inverse Problems in Partial Differential Equations* ed D Colton, R Ewing and W Rundell (Philadelphia, PA: SIAM) pp 101–39
[39] Sylvester J and Uhlmann G 1987 A global uniqueness theorem for an inverse boundary value problem *Ann. Math.* **125** 153–69
[40] Uhlmann G 1998 Inverse boundary value problems for partial differential equations *Doc. Math. J. DMV.* extra volume ICM **III** 77–86
[41] Yorkey T J, Webster J G and Tompkins W J 1987 Comparing reconstruction algorithms for electrical impedance tomography *IEEE Trans. Biomed. Engng* **34** 843–52
[42] Wexler A, Fry B and Neuman M 1985 Impedance-computed tomography algorithm and system *Appl. Opt.* **24** 3982–5